The RAVE Catalog of Stellar Elemental Abundances

Boeche, C.; Siebert, A.; Williams, M.; de Jong, R. S.; Steinmetz, M.; Fulbright, J. P.; Ruchti, G. R.; Bienayme, O.; Bland-Hawthorn, J.; Campbell, R.

Published in:
The Astronomical Journal

DOI:
10.1088/0004-6256/142/6/193

Publication date:
2011

The Astronomical Journal, 142:193 (20pp), 2011 December doi:10.1088/0004-6256/142/6/193

THE RAVE CATALOG OF STELLAR ELEMENTAL ABUNDANCES: FIRST DATA RELEASE

C. Boeche[1], A. Siebert[2], M. Williams[1], R. S. de Jong[1], M. Steinmetz[1], J. P. Fulbright[3], G. R. Ruchti[3], O. Bienaymé[2], J. Bland-Hawthorn[4], R. Campbell[5], K. C. Freeman[6], B. K. Gibson[7], G. Gilmore[8], E. K. Grebel[9], A. Helmi[10], U. Munari[11], J. F. Navarro[12], Q. A. Parker[13,14], W. Reid[13], G. M. Seabroke[15], A. Siviero[1,16], F. G. Watson[14], R. F. G. Wyse[3], and T. Zwitter[17,18]

[1] Leibniz-Institut für Astrophysik Potsdam (AIP), D-14482 Potsdam, Germany
[2] Observatoire Astronomique de Strasbourg, Université de Strasbourg, CNRS, UMR 7550, F-67000 Strasbourg, France
[3] Department of Physics and Astronomy, Johns Hopkins University, Baltimore, MD 21218, USA
[4] Sydney Institute for Astronomy, School of Physics A28, University of Sydney, NSW 2006, Australia
[5] Department of Physics and Astronomy, Western Kentucky University, Bowling Green, KY, USA
[6] Research School of Astronomy and Astrophysics, Australia National University, Weston Creek, Canberra ACT 2611, Australia
[7] Jeremiah Horrocks Institute, University of Central Lancashire, Preston PR1 2HE, UK
[8] Institute of Astronomy, University of Cambridge, Madingley Road, Cambridge CB3 0HA, UK
[9] Astronomisches Rechen-Institut, Zentrum für Astronomie der Universität Heidelberg, D-69120 Heidelberg, Germany
[10] Kapteyn Astronomical Institute, University of Groningen, 9700 AV Groningen, The Netherlands
[11] INAF Osservatorio Astronomico di Padova, Asiago I-36012, Italy
[12] Department of Physics and Astronomy, University of Victoria, Victoria BC V8W 3P6, Canada
[13] Department of Physics and Astronomy, Faculty of Sciences, Macquarie University, Sydney, NSW 2109, Australia
[14] Australian Astronomical Observatory, Epping, NSW 1710, Australia
[15] Mullard Space Science Laboratory, University College London, Holmbury, St. Mary RH5 6NT, UK
[16] Dipartimento di Astronomia, Universitá di Padova, I-35122 Padova, Italy
[17] Faculty of Mathematics and Physics, University of Ljubljana, 1000 Ljubljana, Slovenia
[18] Center of Excellence SPACE-SI, 1000 Ljubljana, Slovenia
Received 2011 June 1; accepted 2011 September 20; published 2011 November 11

ABSTRACT

We present chemical elemental abundances for 36,561 stars observed by the RAdial Velocity Experiment (RAVE), an ambitious spectroscopic survey of our Galaxy at Galactic latitudes $|b| > 25^\circ$ and with magnitudes in the range $9 < I_{\rm DENIS} < 13$. RAVE spectra cover the Ca-triplet region at 8410–8795 Å with resolving power $R \sim 7500$. This first data release of the RAVE chemical catalog is complementary to the third RAVE data release of radial velocities and stellar parameters, and it contains chemical abundances for the elements Mg, Al, Si, Ca, Ti, Fe, and Ni, with a mean error of ∼0.2 dex, as judged from accuracy tests performed on synthetic and real spectra. Abundances are estimated through a dedicated processing pipeline in which the curve of growth of individual lines is obtained from a library of absorption line equivalent widths to construct a model spectrum that is then matched to the observed spectrum via a χ^2 minimization technique. We plan to extend this pipeline to include estimates for other elements, such as oxygen and sulfur, in future data releases.

Key words: catalogs – Galaxy: abundances – Galaxy: evolution – stars: abundances – surveys – techniques: spectroscopic

Online-only material: machine-readable and VO tables

1. INTRODUCTION

Stars inherit the chemical patterns of the interstellar matter from which they were born. At the end of their lives they return their nuclear products to the interstellar medium through stellar winds and supernovae, enriching it with heavier elements. The elemental abundance pattern of every generation of stars thus depends on the previous one and, in time, a sort of "genealogical tree" develops. In principle, this allows for the star formation history of a galaxy to be traced using stellar elemental abundances (Freeman & Bland-Hawthorn 2002).

At the same time, the assembly history of a galaxy also leaves traces in the kinematics of its stars. Indeed, once born, stars behave like a collisionless fluid that spreads through phase space, generally leaving clear tracks of their dynamical origin. For example, disrupted open clusters generate moving groups of stars with similar kinematics that can still be recognized long after disruption (Eggen 1965), while accretion events produce transient stellar streams that closely track the orbit of their progenitor satellites (Helmi et al. 2006).

Chemical and kinematic information, when available, can therefore be used to reconstruct the history of the Milky Way much in the way archaeologists examine relics to recreate the ancient past. The data requirements of this exercise, however, have limited its applicability in the past: assembling a large and homogeneous set of proper motions, distances, radial velocities, and elemental abundances requires large photometric and spectroscopic surveys that have not been feasible until recently.

Spectroscopy has traditionally been the bottleneck, with much of the work on chemical elemental abundances limited to small, biased samples. Until recently, iron abundances ([Fe/H]) had been estimated for samples as large as the ∼16,000 stars of the Geneva–Copenhagen Survey (Nordström et al. 2004), but the numbers of stars with abundances measured for multiple elements were much smaller. Indeed, the largest homogeneous sample available until now was published by Valenti & Fisher (2005), who measured the abundances of five elements in 1040 nearby F, G, and K stars.

Smaller samples, often composed of a few hundred stars or fewer, have also been presented by several authors (Edvardsson

et al. 1993; Fuhrmann 1998, 2008; Luck & Heiter 2006, 2007; Reddy et al. 2006, among others). Larger, but inhomogeneous, data sets have been collated from the literature by Soubiran & Girard (2005) and Venn et al. (2004), who compiled 743 and 821 stars, respectively, and also in the PASTEL catalog (Soubiran et al. 2010), which is a collection of 865 literature studies.

The availability of dedicated telescopes and multi-object spectrographs has radically changed this state of affairs, enabling surveys such as the RAdial Velocity Experiment (RAVE; Steinmetz et al. 2006), and SEGUE (Yanny et al. 2009). Combined, these two surveys have now taken spectra for roughly a million stars. Galactic archaeology has thus become one of the fastest-growing fields of astronomical enquiry, as evidenced by the numerous surveys currently underway or in the advanced planning stages, e.g., *Gaia* (Perryman et al. 2001), LAMOST[19], and HERMES (Freeman & Bland-Hawthorn 2008).

We present here the first release of the chemical catalog for RAVE, an ambitious spectroscopic survey of our Galaxy at Galactic latitudes $|b| > 25^{\circ}$ and magnitudes in the range $9 < I_{\rm DENIS} < 13$. This catalog contains multi-element abundance measurements for 36,561 stars of the Milky Way based on 37,848 RAVE spectra covering the Ca-triplet region at 8410–8795 Å with resolving power $R \sim 7500$. This data release is associated with the RAVE third data release (DR3; Siebert et al. 2011), where further information (kinematics, photometry, etc.) can be found. As of summer 2011, RAVE has taken more than half a million spectra for some 400,000 stars. Abundances for these targets will be published in subsequent data releases.

RAVE (Steinmetz et al. 2006) was first conceived as a radial velocity survey to provide the missing third velocity component for stars in the solar suburb. However, it soon became clear that RAVE spectra carry much more information than just radial velocities. After further development, the RAVE processing pipeline was modified to deliver estimations of the values of stellar parameters like effective temperature, gravity, and metallicity (Zwitter et al. 2008; Siebert et al. 2011).

We take this development one step further here by tackling the measurement of chemical elemental abundances at the medium spectral resolution provided by RAVE data. This feature is shared with other large spectroscopic surveys with limited resolution and spectral coverage, such as *Gaia* and LAMOST. Although high precision is not expected from medium resolution spectroscopy, the availability of hundreds of thousands of RAVE spectra enables the creation of a large and homogeneous catalog of chemical abundances suitable for statistical investigation.

The RAVE chemical pipeline measures abundances for seven elements: Mg, Al, Si, Ca, Ti, Fe, and Ni. Homogeneity is assured by an automated processing pipeline that measures abundances assuming the stellar parameters computed by the RAVE pipeline described in Siebert et al. (2011). RAVE stars have astrometry from different sources like *Tycho*2 (Høg et al. 2000), PPMX (Roeser et al. 2008), and UCAC2 (Zacharias et al. 2004). These, together with RAVE radial velocities and distance estimates (Breddels et al. 2010; Zwitter et al. 2010; Burnett et al. 2011), yield three-dimensional positions and velocities. Combining this information with chemical abundances results in a unique chemo-kinematic data set suitable for investigations of the formation history of the Galaxy.

This paper is structured as follows. In Section 2, we present the chemical processing pipeline, detailing how the chemical elemental abundances are measured. Tests to establish the accuracy and reliability of the results are detailed in Section 3, while in Section 4 we discuss our method of measurement, and in Section 5 we present the RAVE chemical catalog. In Section 6 we outline our conclusions.

2. THE PIPELINE

The RAVE chemical abundance pipeline uses a different approach to classical elemental abundance estimation methods. These methods either (1) measure equivalent widths (EW)s and infer elemental abundances from the curves-of-growth (COGs) or (2) synthesize spectra with varying elemental abundances to find the best match between the synthetic and observed spectra. The first method cannot be successfully applied to the RAVE spectra because it requires isolated lines for precise EW measurements and, at the medium resolution of RAVE, most of the lines are instrumentally blended. Also, the second method is computationally too expensive as it requires the synthesis of several spectra ~400 Å wide, each having hundreds of lines.

The adopted method can be considered a hybrid approach, measuring the elemental abundances by fitting the spectrum with a model constructed with lines of known EWs. The construction of the model is robust and fast, with the elemental abundances determined by a χ^2 minimization routine. The drawback of this method is that the EWs of the lines are computed by neglecting the opacity of the neighboring lines. This may overestimate the EWs, leading in some cases to underestimated elemental abundances. We show below that this effect is small for most of the lines in the RAVE wavelength range.

2.1. Procedure

The chemical pipeline utilizes RAVE reduced spectra and their stellar parameters, such as effective temperature ($T_{\rm eff}^{\rm RAVE}$), gravity ($\log g^{\rm RAVE}$), and metallicity ($[{\rm m/H}]^{\rm RAVE}$), returned by the RAVE pipeline (described in Siebert et al. 2011).[20] The pipeline also uses an EW library based on the RAVE line list. The RAVE line list contains 604 known absorption lines identified in the RAVE wavelength range (Section 2.2). The EW library contains the EWs of absorption lines for every point on the $T_{\rm eff}$, $\log g$, and [m/H] grid (Section 2.3), which accounts for the variation of the EW with the stellar parameters. Variations of EW with elemental abundances are then further calculated for each point of this grid, for five different abundance levels in the range $[-0.4, 0.4]$ with respect to the value of metallicity [m/H].

The pipeline contains some auxiliary codes to (re)normalize the spectrum and detect spectral defects like bad normalization, cosmic rays, and other unwanted features.

The pipeline algorithm can be outlined as follows.

1. Upload the normalized, RV corrected, and wavelength calibrated spectrum and the estimated stellar parameters $T_{\rm eff}^{\rm RAVE}$, $\log g^{\rm RAVE}$, $[{\rm m/H}]^{\rm RAVE}$.
2. Upload the RAVE line list from the EW library and the corresponding EWs for the stellar parameters at the five different abundance levels.
3. Extract a shorter line list of those lines which, at the estimated stellar parameters, have large enough EWs to be visible above the noise.
4. Fit the strong lines and correct the continuum.

[19] http://www.lamost.org/website/en

[20] $[{\rm m/H}]^{\rm RAVE}$ indicates the uncalibrated metallicity as defined in Zwitter et al. (2008).

5. Construct the COGs of the lines by fitting a polynomial function through the five EW abundance points.
6. Create the model by assuming a Gaussian profile for each line and summing these profiles together.
7. Vary the chemical elemental abundances to obtain different models by changing the EWs of the lines according to their COG.
8. Minimize the χ^2 between the models and the observed spectrum to find the best-matching model.

In the following we give further details pertaining to these steps.

2.2. Line List and Constraining the Oscillator Strength

The RAVE line list contains 604 absorption lines identified in spectra of the Sun and Arcturus. The lines correspond to the element species N I, O I, Mg I, Al I, Si I, S I, Ca I, Ti I, Ti II, Cr I, Fe I, Fe II, Co I, Ni I, Zr I, and to the CN molecule. In order to get precise chemical elemental abundances from the EWs, we first need reliable atomic parameters for the lines. A critical parameter is the oscillator strength (gf, often expressed as logarithm $\log gf$). If precise laboratory measurements are missing for the $\log gf$ values then they are obtained through an inverse spectral analysis to obtain "astrophysical $\log gf$s." This is the case for the RAVE wavelength region, where the Vienna Atomic Line Database (VALD; Kupka et al. 1999) reports that only 11 Fe I lines have laboratory oscillator strength measurements. The Sun's and Arcturus's spectra were synthesized and the $\log gf$ values for each line were obtained using an automated procedure which varies the $\log gf$s so as to match both spectra simultaneously. For the synthesis we adopted solar abundances as given by Grevesse & Sauval (1998). They will be the zero point of the abundances of this work. The details of the procedure are outlined in Appendix A.

The pipeline makes use of a shorter working line list which contains the lines strong enough to be visible above the noise. The lines deemed visible are those satisfying

$$\mathrm{EW(m\AA)} > 2 \cdot \frac{1}{\mathrm{STN}} \cdot d \cdot 1000,$$

where STN is the signal-to-noise ratio[21] and d is the spectral dispersion (for RAVE spectra $d = 0.4$ Å pixel^{-1}). Other lines can blend with these visible lines, contributing to their flux absorption and changing their apparent EW. We therefore added to the working line list all those lines having EW > 1 mÅ and being closer than 0.6 Å (1.2 Å is the FWHM of a typical RAVE spectrum) to the visible lines.

2.3. The EW Library and COG Computation

In order to compute the line COGs we built an EW library with the RAVE line list for 30, 640 atmosphere models. The EWs were computed using the LTE line-analysis software MOOG (Sneden 1973) and the ATLAS9 model atmosphere grid (Castelli & Kurucz 2003). As the spacing of the ATLAS9 grid is different to our requirements, we linearly interpolated the ATLAS9 grid to produce our own grid, covering the $T_{\rm eff}$ range [3600, 7600] K in steps of 100 K, gravity range [0.0, 5.0] dex in steps of 0.2 dex, and metallicities in the range $[-2.5, +0.5]$ dex in steps of 0.1 dex. We did not compute the EWs for atmospheres with $T_{\rm eff} > 5100$ K and $\log g < 1.0$ (hot supergiants), because MOOG does not produce results for these parameters and furthermore there are no such stars in our catalog. For every atmosphere model we computed the EWs of the lines for five abundance levels with respect to iron: $[\mathrm{X/Fe}] = -0.4, -0.2, 0.0, 0.2, 0.4$ dex assuming $[\mathrm{Fe/H}] = [\mathrm{m/H}]$. The whole EW library consists of 145, 080 files. To obtain EWs for stellar parameters between the grid points of the EW library we linearly interpolate the closest points on the grid.

[21] In the following, we will use STN to indicate the signal-to-noise ratio as computed in Siebert et al. (2011) whereas S/N will be used with the usual meaning given in spectrophotometry.

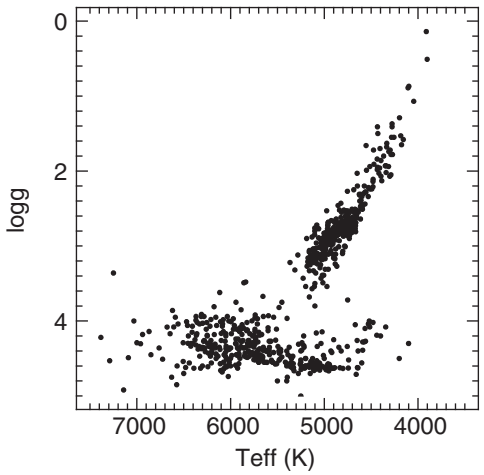

Figure 1. Distribution on ($T_{\rm eff}$, $\log g$) plane of 712 stars observed spectroscopically at high resolution.

2.4. Microturbulence

The EW computation requires a value of the microturbulence ξ for each atmosphere model. For high-resolution data ξ is typically determined by measuring the EWs of Fe I lines and changing ξ until the iron abundances inferred from strong and weak lines agree. As we do not measure individual EWs for our spectra we cannot use this procedure, but instead rely on relations giving ξ as a function of the stellar parameters. Such relations have been derived by Edvardsson et al. (1993), Reddy et al. (2003), and Allende Prieto et al. (2004), where ξ is given as a function of $T_{\rm eff}$ and $\log g$. Unfortunately, these results cover only specific regions of parameter space (e.g., hot dwarfs or cold giants). Thus, we derived our own relation covering a wide a range of $T_{\rm eff}$ and $\log g$. To do so we made use of literature results from high-resolution spectroscopy that report both stellar parameters and ξ of their stellar samples. We collected data for 712 giants and dwarfs spanning a wide range in $T_{\rm eff}$ and $\log g$ from Luck & Heiter (2006, 2007), Bensby et al. (2005), Fuhrmann (1998), Fulbright et al. (2006), and Allende Prieto et al. (2004). Figure 1 displays the coverage in the $T_{\rm eff}$–$\log g$ plane for the sample. A third-degree polynomial fit was used to obtain the microturbulence dependence on gravity and effective temperature. Appendix B gives the coefficients of this polynomial fit, $\xi_{\rm poly}$.

Figure 2 compares the Allende Prieto et al. (2004) law with $\xi_{\rm poly}$. Uncertainties of $\sigma_\xi = 0.32$ km s^{-1} in our polynomial law translate approximately into $\sim$0.04 dex elemental abundance uncertainties for dwarfs stars (as estimated by Reddy et al. 2003 and Mishenina et al. 2004).

2.5. Continuum Re-normalization and Strong Line Fitting

Before measuring EWs, the spectrum's continuum needs to be re-normalized and its strong lines fitted. While the spectrum

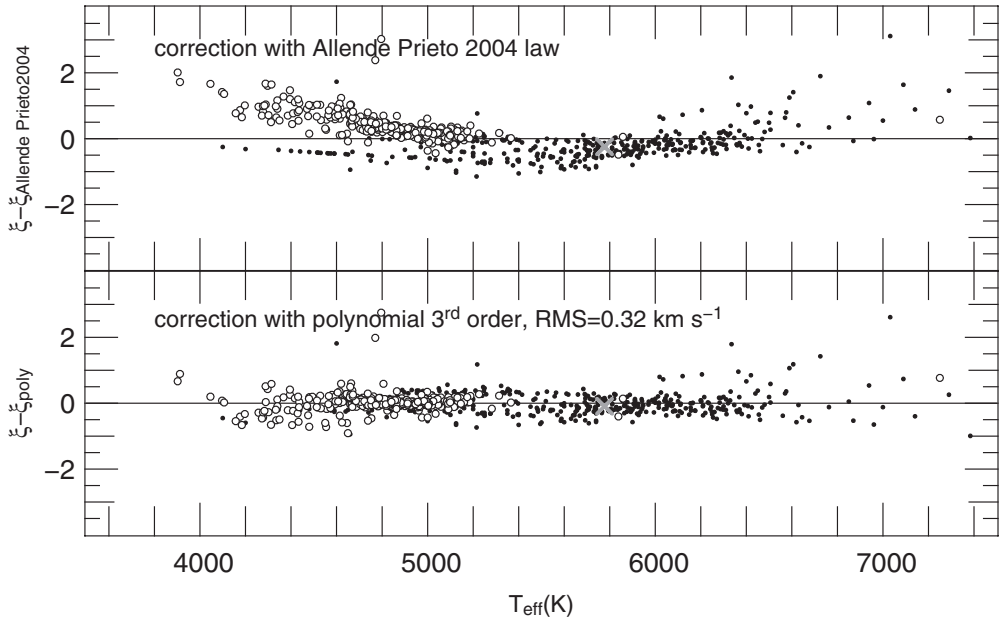

Figure 2. Top panel: residuals between measured microturbulence ξ and computed ξ with the Allende Prieto et al.'s formula for 712 stars. Bottom panel: residuals between measured ξ and computed by a third-degree polynomial function. Solid and open points represent dwarf and giant stars, respectively. The gray cross represents the Sun.

is continuum normalized by the RAVE pipeline, we have found that this normalization is not rigorous enough for elemental abundance estimation: the RAVE pipeline employs a third-order spline function to fit the continuum, leaving behind fringing effects on scales of less than 50 Å wide seen in some RAVE-normalized spectra. The chemical pipeline performs a new normalization to remove such unwanted features, fitting the continuum and the strong Ca II and H I Paschen lines. These strong lines are then excluded from the measurement process because they are difficult to fit properly. The pipeline then considers as "continuum" the fit to the classical continuum plus the strong lines, and by comparison with this level the metallic lines are measured.

Before applying the continuum correction we estimate a preliminary metallicity, which we call $[m/H]^{est}$ to distinguish it from the final metallicity $[m/H]^{chem}$. This preliminary metallicity is required because the intensity of the absorption lines must be known in order to subtract them. When they are subtracted the continuum level can then be seen. However, in order to measure the intensity of a line one must know where the continuum lies. The continuum level is therefore determined iteratively, starting with the normalization of the RAVE pipeline and measuring the line intensities using the chemical elemental abundances estimation subroutine (see Section 2.6), with the difference that all the abundances vary together as one variable $[X/H] = [m/H]^{est}$. Wavelength intervals ∼20 Å wide centered on the strong lines are avoided as the large wings of these lines can affect the results of the χ^2 determination of the metallicity. The best-match $[m/H]^{est}$ is then used to synthesize the metallic lines, which are then subtracted before the strong lines are fit.

Fitting the continuum is performed in four steps, summarized below and illustrated in Figure 3 from top to bottom.

1. Perform a preliminary metallicity and subtract the metallic lines (gray line in panel (a), Figure 3).
2. Fit the strong lines with a Lorentzian profile for Ca II and a Gaussian profile for H I and subtract them (gray line in panel (b), Figure 3).

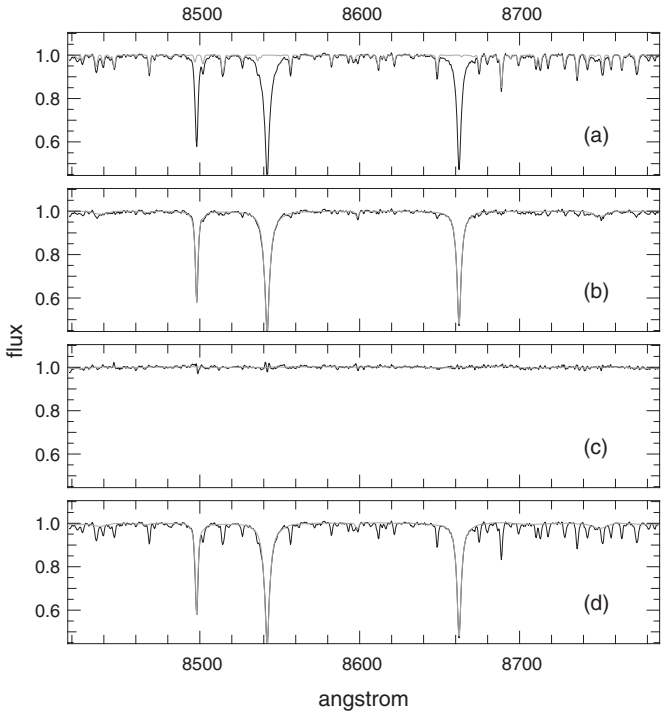

Figure 3. Black line: RAVE spectrum of the Sun. (a) Metallic lines fitting. (b) Strong line fitting. (c) Continuum fitting. (d) The gray line is the sum of the gray lines in panels (b) and (c). This curve is used as the continuum line from which we estimate the chemical elemental abundances.

3. Estimate the continuum profile by box-car smoothing what remains (gray line in panel (c), Figure 3).
4. Add the strong lines and the continuum together to obtain the new "continuum" (gray line in panel (d), Figure 3).

2.6. Chemical Elemental Abundance Estimation

The chemical pipeline uses the parameters $T_{\rm eff}^{\rm RAVE}$ and $\log g^{\rm RAVE}$ for the elemental abundance estimation. The observed

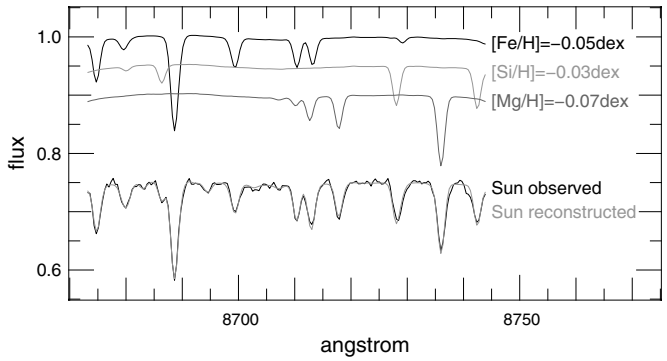

Figure 4. Once the abundances of Fe, Si, and Mg are fixed their absorption lines can be synthesized (gray lines on the top). By summing them together we obtain the gray line on the bottom, which is the model spectrum of the Sun. The black line is the Sun's spectrum reflected by the Moon and observed by RAVE.

spectrum is fit by a model spectrum first obtained by subtracting the flux absorbed by the metallic lines to that derived above in Section 2.5, i.e., the strong lines + continuum fit (gray line in panel (d), Figure 3). The absorption lines are assumed to have Gaussian profiles, and as the instrumental profile is dominant with respect to the line profile, we use the same FWHM for all lines. However, this FWHM is varied and optimized during the χ^2 minimization process.

The pipeline computes the COG of the lines by using the EWs at five levels of abundances ([X/Fe] = −0.4, −0.2, 0.0, 0.2, 0.4 dex, assuming [Fe/H] = $[m/H]^{RAVE}$) from the EW library. For every line, the five EW points are fit with a third-order polynomial function, which serves as the COG. However, these polynomial functions represent only part of the COGs and will diverge if extrapolated too far beyond the five levels in the EW library. To avoid such divergences we limit accepted abundance results to those in the range $-0.6 \leqslant [X/Fe] \leqslant +0.6$.[22]

Using the COGs the pipeline then creates the model spectrum, using [X/H] = $[m/H]^{RAVE}$ as a first guess for the metallicity. It computes the χ^2 between the observed spectrum and the model and, through a minimization process, changes the elemental abundances [X/H] until the best match (minimum χ^2) with the observed spectrum is reached. The minimization process is performed with 15 variables: 13 elemental abundances, one molecule, and the instrumental FWHM of the lines.

Figure 4 shows the best-match model spectrum of the Sun and compares it with the observed one. The three spectra on the top show how the model spectrum is built up: the spectra of three elements (Fe, Si, Mg) at parameters $T_{\rm eff} = 5861$ K and $\log g = 4.54$ are generated according to the estimated elemental abundances and added together to construct the solar spectrum.

This methodology has a drawback: the computed COG of any absorption line neglects the opacity of the neighboring lines, leading to an overestimation of the EW of blended lines and so an underestimation of the elemental abundances. This systematic originates from the EW library created by using the MOOG's driver "ewfind," which computes the expected EW of the lines as if they were isolated. In order to minimize this systematic error we apply a correction coefficient to reduce the EWs of lines which are physically blended. The corrected EW is given by

$$\mathrm{EW}_{\rm corr} = \mathrm{EW} \cdot \mathrm{coeff} \cdot \mathrm{cont}, \quad (1)$$

where the coefficient

$$\mathrm{coeff} = 1 - \sum_{i}^{\text{neighbor}<0.2\,\text{Å}} \mathrm{EW}_i/2.50/\mathrm{dispersion}$$

is computed by considering all the neighboring lines within 0.2 Å of the line of interest. The dispersion is expressed in Å pixel^{-1} and cont is the value of the continuum (gray line in panel (d) of Figure 3) at the central wavelength of the line. The multiplication of the EW by cont in Equation (1) corrects for the effects of strong lines (such as Ca II) if the line of interest lies within their large wings. This correction reduces the systematic error in the abundances from ∼−0.15 dex to ∼−0.1 dex or less for most elements (see details in the following sections, where quality checks are outlined).

2.7. Spectrum Quality Determination: The frac Parameter

Roughly 25% of RAVE spectra are affected by defects like fringing or cosmic rays that cannot be removed by continuum correction (they usually affect regions smaller than 100 Å). In order to determine the locus and size of the defect we define the flux residual between the observed and the best-match model for the ith pixel with

$$r(i) = f_{\rm model}(i) - f_{\rm obs}(i),$$

where f is the flux of the spectra, and we use the following algorithm (also used in Siebert et al. 2011).

1. Consider the interval $I_j = [j - 10, j + 10]$ centered on the pixel j. Compute

$$\tilde{\chi}^2(j) = \frac{1}{\max(I_j) - \min(I_j)} \cdot \sum_{i=\min(I_j)}^{\max(I_j)} \left(\frac{r(i)}{\sigma}\right)^2,$$

$$\psi(j) = \frac{1}{\max(I_j) - \min(I_j)} \sum_{i=\min(I_j)}^{\max(I_j)} r(i),$$

   where $\tilde{\chi}^2(j)$ is the reduced χ^2 and $\psi(j)$ is the estimation of the area between the observed and model spectra. σ is the inverse of the signal-to-noise (STN) ratio.
2. If $\tilde{\chi}^2(j) > 2$ and $\psi(j) > 2 \cdot \sigma$ then the pixels in the interval I_J are labeled as a defect.

The process is repeated for all the pixels of the spectrum, resulting in an array of 0 and 1, with 1 label indicating non-defective pixels. The fraction of pixels that are non-defective is then denoted with the *frac* parameter (i.e., the higher the *frac* parameter, the better the quality of the spectrum). We deem spectra with $frac < 0.7$ as overly affected by fringing/cosmic ray defects and exclude these spectra from our analysis.

3. VALIDATION AND ACCURACY

There are several sources of error that affect the elemental abundances measurement process. For example, there are uncertainties in (1) the oscillator strength values, (2) the continuum normalization, (3) the stellar parameters, (4) microturbulence, (5) uncertainties due to local line opacity neglected by the pipeline, (6) neglect of non-LTE effects, and (7) photon shot noise. These sources of errors interact in a complex fashion, making the error estimation process quite challenging. To establish the capability of the pipeline to derive the

[22] Abundances beyond this limit can be due to photon noise stronger than the absorption lines or to peculiar abundances. The two cases cannot be distinguished by the chemical pipeline.

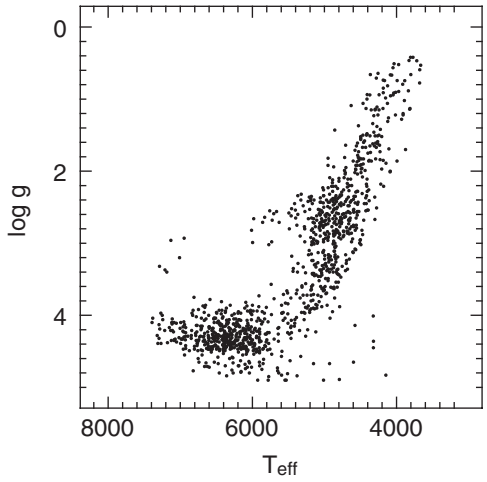

Figure 5. Distribution of the synthetic spectra sample on the stellar parameters plane $T_{\rm eff}$ and $\log g$.

chemical elemental abundances we ran a series of tests on synthetic and real spectra for which stellar parameters and elemental abundances are well known. The results are presented below.

3.1. Chemical Elemental Abundances Accuracy from Synthetic Spectra

We ran the pipeline on a sample of 1353 synthetic spectra to which three intensity levels of artificial noise were added, testing the accuracy of the results at S/N = 100, 40, and 20. To make the sample as realistic as possible, the spectra have been synthesized with distributions of $T_{\rm eff}$ and $\log g$ from a mock sample of RAVE observations (M. Williams 2009, private communication) created by using the Besançon model (Robin et al. 2003). The $T_{\rm eff}$ versus $\log g$ distribution of the sample is shown in Figure 5.

Each spectrum of the sample had the elemental abundances of one of the stars from the Soubiran & Girard (2005) catalog, ensuring realistic distribution of the chemical abundances. As our line list has only eight elements in common with the Soubiran & Girard catalog, we assigned the elemental abundance [X/H] = [Fe/H] to the elements Cr, Co, Ni, Zr. We also assigned [X/H] = [α/H] to C, N, O, Mg, Al, Si, S, Ca, Ti when the measurement of one of these elements was missing. The spectra were synthesized using the code MOOG at resolution 0.01 Å pixel^{-1} and degraded to RAVE resolution (0.4 Å pixel^{-1}, 1.4 Å FWHM).

The first test was performed by adopting the stellar parameters $T_{\rm eff}$, $\log g$, and [m/H] of the synthetic spectrum in order to evaluate the accuracy of the elemental abundance measurements of the pipeline alone. The results are illustrated in Figure 6. For the second test we added uncertainties to the stellar parameters so as to simulate real RAVE spectra. Following the typical RAVE errors, we added a random Gaussian error with standard deviation 300 K in $T_{\rm eff}$, 0.5 dex in $\log g$, and 0.3 dex in [m/H] to the correct parameters and ran the pipeline adopting such "wrong" parameters. For the sake of brevity and clarity we present only the results for the seven most reliable elements (see also Figure 7).

3.1.1. Results Assuming No Error in the Stellar Parameters

Results at S/N = 100. With no errors added to the stellar parameters the residuals between measured and expected elemental abundances [X/H] have a systematic error of $\simeq -0.10$ dex and standard deviation $\sigma \simeq 0.10$ dex or smaller (see Figure 6), with a slight variation from element to element. The relative enhancement [X/Fe] shows a small ($\simeq -0.10$ dex) systematic error at high [X/Fe].

Results at S/N = 40. The elemental abundance residuals have $\sigma \simeq 0.10$–0.20 dex depending on the element and show the same systematics seen with S/N = 100, but slightly less pronounced.

Results at S/N = 20. At this S/N the pipeline can still estimate abundances of Fe, Al, and Si and the relative enhancement to iron [X/Fe], but with $\sigma \simeq 0.2$–0.3 dex. Other elements like Mg and Ti exhibit larger systematic errors. An α-element abundance estimated as the average of Mg and Si still yields reliable results with an error of $\sigma \simeq 0.2$ dex. Elements such as Ca and Ni cannot be reliably measured because the lines are too weak to be detected.

We found correlations between stellar parameters and elemental chemical abundances obtained. In particular, the abundances correlate with $T_{\rm eff}$ (Figure 8). This is very likely due to continuum correction, which can appear lower than the real level in spectra crowded of lines, as in cold giants stars.

3.1.2. Results Including Errors in the Stellar Parameters

Results at S/N = 100. When errors are added to the stellar parameters the elemental abundances [X/H] are affected to the level of $\sigma \simeq 0.15$–0.20 dex for elements like Mg, Al, Si, Ca, Fe, Ni. Titanium abundances show clear systematic errors, being overestimated at high abundance and underestimated at low abundance. Enhancements relative to Fe, [X/Fe], have errors $\sigma < 0.2$ dex and little sign of systematic errors for most of the elements.

Results at S/N = 40. The elemental abundance errors are in the range $\sigma \simeq 0.15$–0.30 dex depending on the element. The relative elemental abundances [X/Fe] are reliable with errors $\sigma \simeq 0.2$ dex.

Results at S/N = 20. At this S/N the pipeline can still estimate abundances of Fe, Al, and Si and the relative enhancement with respect to iron [X/Fe] even with an error of $\sigma \simeq 0.2$–0.3 dex. Other elements like Mg and Ti show systematic errors. An α-element abundance computed by averaging Mg and Si yields reliable results with an error of $\sigma \simeq 0.2$ dex. Elements such as Ca and Ni cannot be reliably measured because the lines are too weak to be detected.

As could be expected, there is a correlation between errors in stellar parameters and errors in the elemental abundance estimates. Figure 9 highlights these correlations, showing that most of the elemental abundance errors are correlated with $T_{\rm eff}$ errors. In general, an overestimate in $T_{\rm eff}$ corresponds to an overestimate in abundance, since most of the lines have smaller EW at higher $T_{\rm eff}$. Only weak correlations with $\log g$ and [m/H] errors are evident.

3.2. The Accuracy of Elemental Abundance Estimates from Real Spectra

The initial RAVE input catalog had no stars whose chemical elemental abundances were known to high accuracy to compare with the results of our pipeline. To create a comparison data set of real stars, we therefore observed 104 stars chosen from Soubiran & Girard (2005, hereafter SG05), a collection of high-precision elemental abundance measurements from the literature. Since these are bright stars, most of the RAVE spectra have S/N > 100 and therefore the accuracy in our abundance estimates is representative of the high S/N case. Ruchti et al.

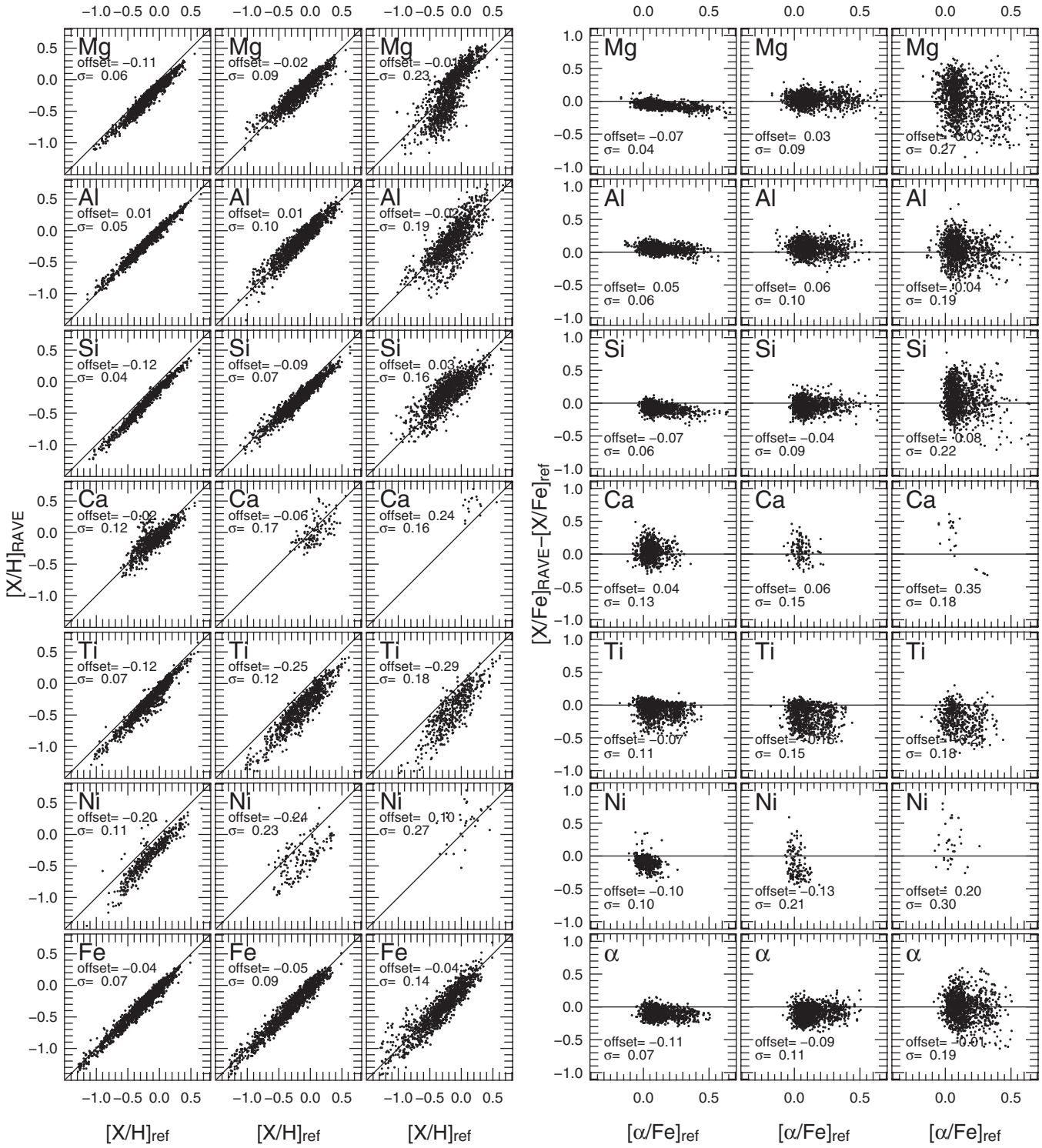

Figure 6. Left: expected elemental abundances [X/H] (*x*-axis) vs. measured elemental abundances (*y*-axis) for the sample of synthetic spectra at S/N = 100, 40, 20 (for the left, middle, and right columns, respectively) and assuming no errors in stellar parameters. Right: as in left panels but for the expected enhancement [X/Fe] (*x*-axis) and the residuals measured minus expected (*y*-axis). Offsets and standard deviations are reported in the panels.

(2010, hereafter R10) have also re-observed 243 RAVE stars at high-resolution and measured stellar parameters and chemical elemental abundances. The RAVE spectra of these stars have S/N between 30 and 90 and therefore we can use them to test the accuracy of our procedure for intermediate S/N.

We have seven elements in common with SG05 and five elements with R10 (Fe, Mg, Si, Ca, and Ti). However, for the latter we could only compare four elements because the weak Ca I lines were not strong enough in the RAVE spectra to be measured by the pipeline. As with synthetic spectra, we ran a first test by adopting the high-resolution stellar parameters to evaluate the performance of the pipeline alone and then ran a second test by using the RAVE stellar parameters, which have larger uncertainties relative to the high-resolution data.

The results of the first test are shown in Figure 10 where the gray dots and black "+'s" correspond to SG05 and R10,

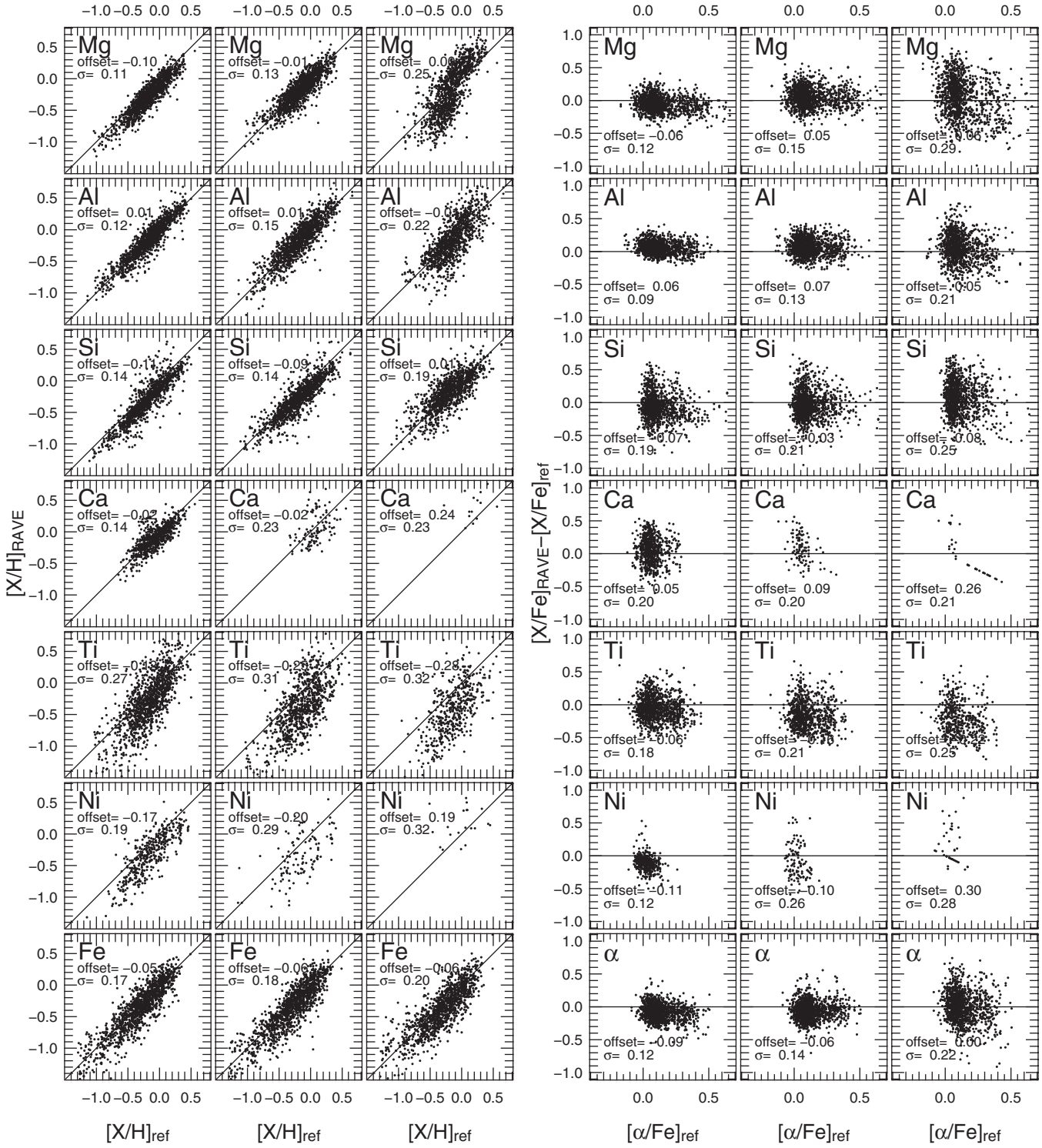

Figure 7. Same as Figure 6 but with noisy stellar parameters to simulate the RAVE stellar parameters of the RAVE archive.

respectively. When the high-resolution stellar parameters are adopted the chemical pipeline's elemental abundances agree with the SG05 and R10 results to within ∼0.15 dex on average. The smaller dispersion of the SG05 stars around the one-to-one correspondence line compared to R10 is due to the higher S/N of the RAVE spectra of these stars. All elements are typically underestimated by ∼0.1 dex, an offset that is roughly constant across the entire abundance range [−2.0, +0.5] dex. The α-enhancement (Figure 11) is estimated well for all but [α/Fe] > 0.4 dex, where there is a small systematic bias of ∼0.1 dex.

When the RAVE stellar parameters are adopted (the "second test," Figure 12) the dispersion in our elemental abundances compared to the published values increases to ∼0.2–0.3 dex on average, depending on the element. In Table 1 we report the mean and standard deviation after grouping the sample in dwarf and giant stars separately. The larger dispersion at low abundances ([X/H] < −1.0 dex) is very likely due to the fact that estimating precise stellar parameters on such spectra is challenging due to the few and weak visible absorption features (excluding for the Ca II triplet, which is not measured).

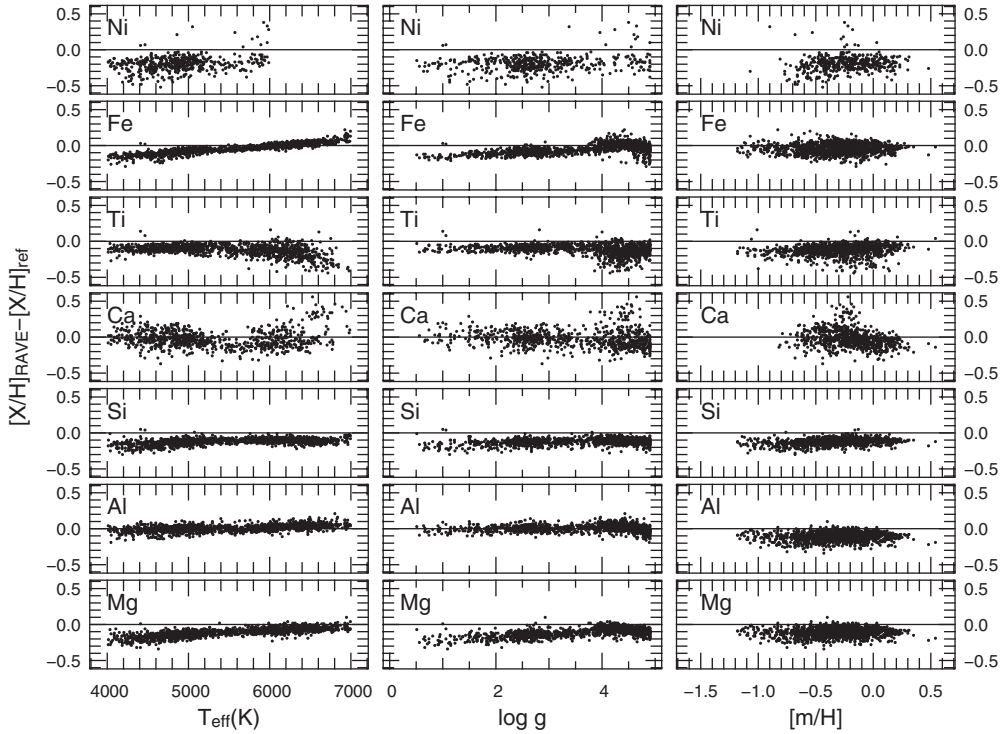

Figure 8. Correlation between the elemental abundance residuals measured minus expected (*y*-axis) and the stellar parameters (*x*-axis) at S/N = 100.

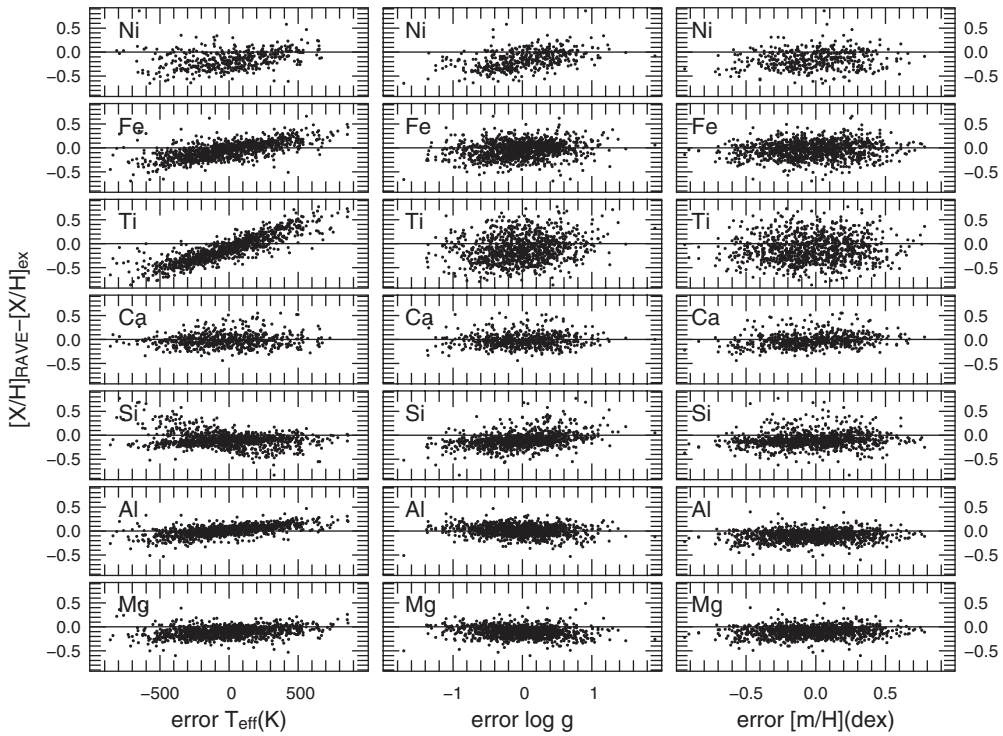

Figure 9. Correlation between the elemental abundance residuals measured minus expected (*y*-axis) and the stellar parameter errors (*x*-axis) at S/N = 100.

The enhancement estimates ([X/Fe], see Figure 13) are accurate to within ∼0.3 dex. At high enhancements, abundances are systematically underestimated by ∼0.1–0.2 dex, depending on the element. However, as we are comparing our measurements with other authors' (high resolution) measurements, the variance of the residuals is the quadratic sum of the variances of our and the high-resolution results. This means that the standard deviations reported in Figures 12 and 13 represent a conservative estimate of the expected RAVE errors.

3.3. Internal Errors from Repeat Observations

In order to take into account the effect of binary stars, RAVE observes some stars (∼5% of the whole sample) more than once. In this chemical catalog, 964 stars have been observed

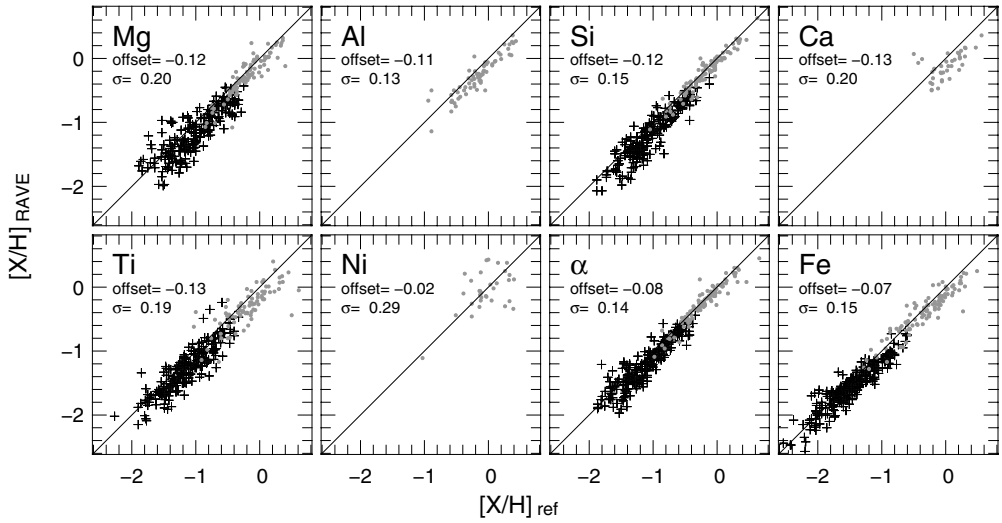

Figure 10. Comparison between high-resolution elemental abundance ($[X/H]_{ref}$) from the literature (x-axis) and RAVE elemental abundances (y-axis) for the SG05 sample (98 stars, gray dots) and the R10 sample (243 stars, black "+'s"). For these measurements we adopted the values of T_{eff} and $\log g$ from the high-resolution data (first test).

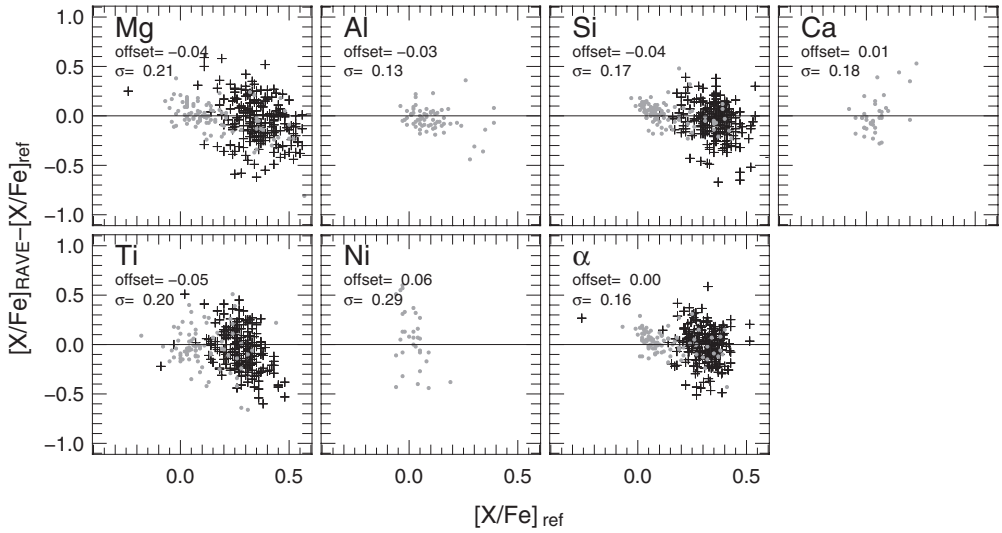

Figure 11. Relative elemental abundance residuals RAVE-minus-high-resolution (y-axis) vs. high-resolution measurements ($[X/Fe]_{ref}$). For these measurements we adopted the values of T_{eff} and $\log g$ from the high-resolution data (first test). The symbols are as in Figure 10.

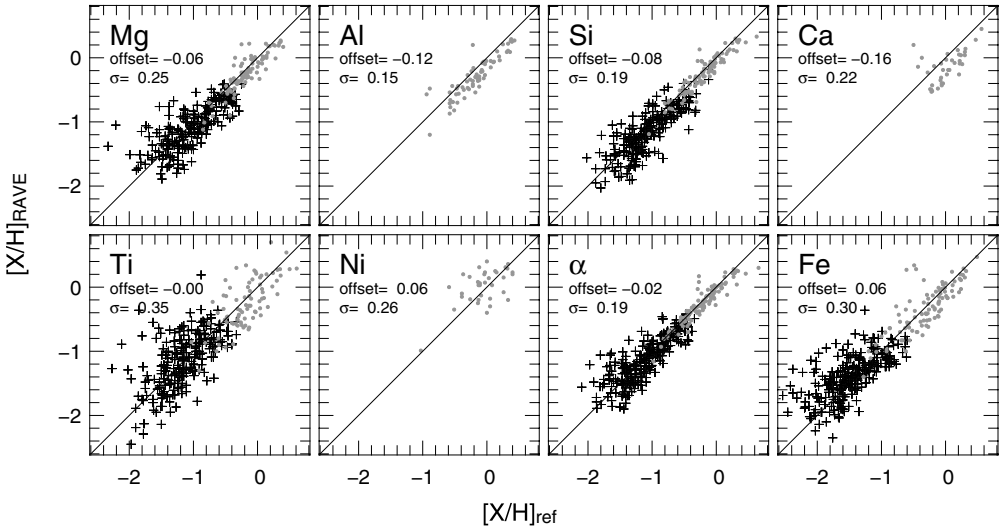

Figure 12. Same as Figure 10 but adopting T_{eff} and $\log g$ from the RAVE data (second test).

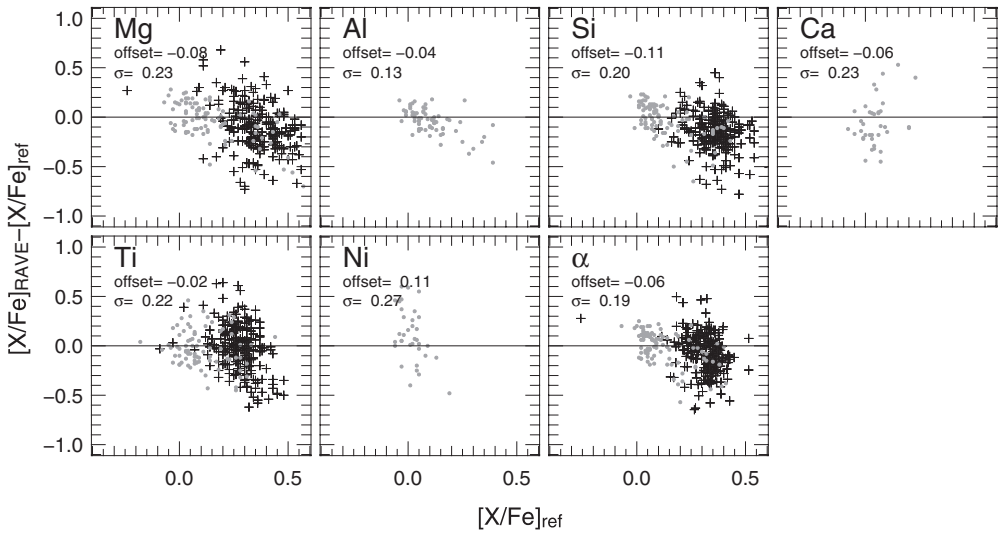

Figure 13. Same as Figure 11 but adopting $T_{\rm eff}$ and $\log g$ from the RAVE data (second test).

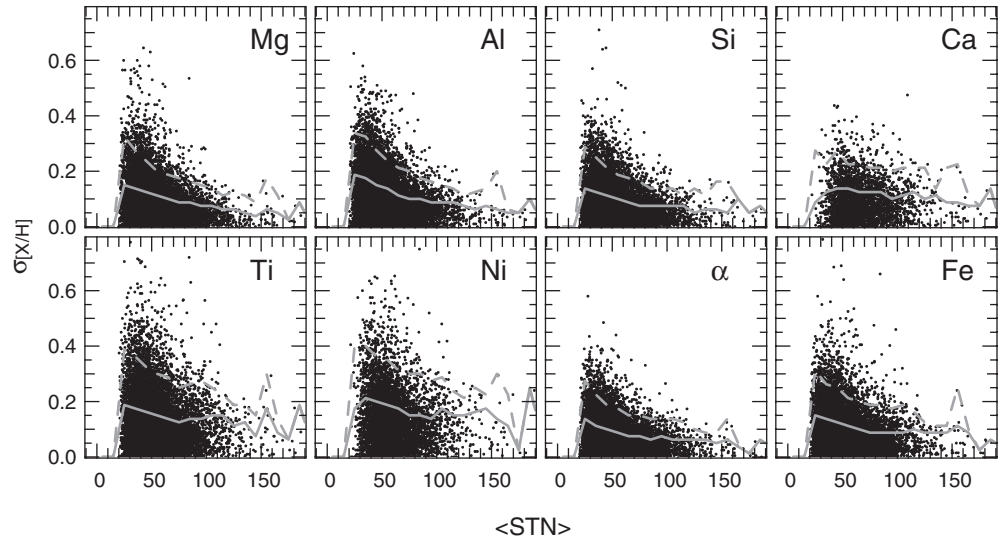

Figure 14. Expected internal errors of the chemical elemental abundances, estimated via standard deviations of the abundances from repeat observations. For a more robust statistic we used 30,821 spectra of 12,504 stars of the RAVE internal data release. The solid gray line represents the 1σ abundance error limit, i.e., 68% of the stars lie under the line for each STN bin, whereas the dashed gray line represents the 2σ limit. For this sample 9469 stars have two observations, 1286 have three, 1060 have four, 473 have five, 153 have six, 33 have seven, 11 have eight, 11 have nine, 4 have ten, and 4 have eleven observations.

Table 1
Mean and Standard Deviation of the Residuals between Measured and Expected Elemental Abundances Obtained by Using the High Resolution Stellar Parameters (Left) and the RAVE Parameters (Right) for 347 Standard Stars

Element Residuals	High Resolution Stellar Parameters				RAVE Stellar Parameters			
	Giants		Dwarfs		Giants		Dwarfs	
	Mean	σ (dex)	Mean	σ (dex)	Mean	σ (dex)	Mean	σ (dex)
[Mg/H]–[Mg/H]$_{\rm ex}$	−0.15	0.21	−0.08	0.14	−0.05	0.28	−0.06	0.15
[Al/H]–[Al/H]$_{\rm ex}$			−0.11	0.13			−0.11	0.15
[Si/H]–[Si/H]$_{\rm ex}$	−0.15	0.15	−0.04	0.09	0.11	0.21	−0.03	0.14
[Ca/H]–[Ca/H]$_{\rm ex}$			−0.13	0.20			−0.16	0.22
[Ti/H]–[Ti/H]$_{\rm ex}$	−0.14	0.17	−0.12	0.22	0.10	0.36	−0.03	0.30
[Fe/H]–[Fe/H]$_{\rm ex}$	−0.08	0.15	−0.06	0.15	0.07	0.30	0.04	0.31
[Ni/H]–[Ni/H]$_{\rm ex}$			−0.02	0.29			0.06	0.26
[α/H]–[α/H]$_{\rm ex}$	−0.10	0.15	−0.04	0.10	−0.02	0.21	−0.02	0.15

Notes. We computed the values for giants ($\log g < 3.5$) and dwarfs ($\log g \geqslant 3.5$) separately. The two groups are also representative of stars with $T_{\rm eff} < 5500$ K and intermediate STN (R10 stars), and stars with $T_{\rm eff} > 5500$ K and high STN (SG05 stars).

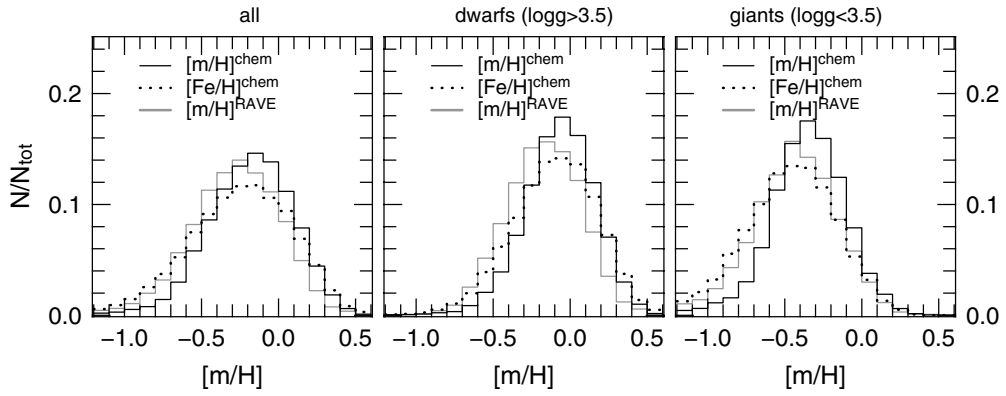

Figure 15. Comparison between $[m/H]^{chem}$ (black line) $[Fe/H]^{chem}$ (dotted line) and $[m/H]^{RAVE}$ (non-calibrated metallicity, gray line) distributions for the whole sample (37848 spectra, left panel), dwarf (middle panel), and giant stars (right panel).

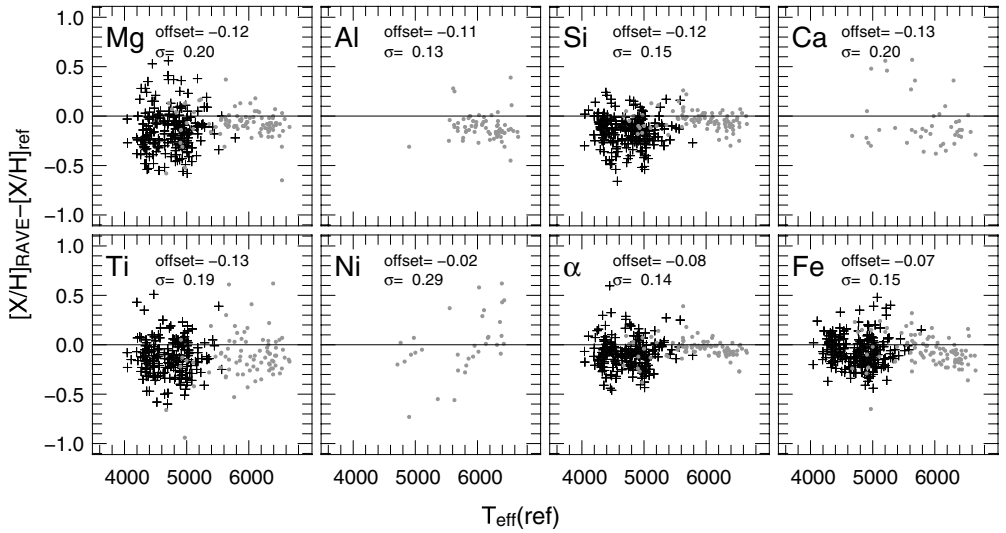

Figure 16. Residuals between measured and expected elemental abundances as a function of T_{eff}. For these measurements we adopted high-resolution stellar parameters. The symbols are as in Figure 10.

twice, 90 thrice, and 67 four times. Multiple observations are also useful to estimate the internal error by comparing the results obtained from different spectra of the same object. A fair comparison would require that the repeated observations of an object have the same S/N. Unfortunately, due to variable atmospheric conditions the spectra often have different S/N values. We therefore averaged the STNs of the spectra for each object and computed the corresponding standard deviations of the elemental abundances. In this way we could assess the magnitude of internal errors in our procedure as a function of STN. In Figure 14 we plot the results for 12,504 RAVE stars having multiple observations, where we use the RAVE internal data release as it has a substantially larger number of stars. For all the elements the 1σ confidence line (gray solid line) lies below 0.2 dex and hovers around ∼0.1 dex for STN > 80.

3.4. $[m/H]^{RAVE}$ versus $[m/H]^{chem}$: a Comparison

In Figure 15 we compare the distributions of $[m/H]^{RAVE}$, $[m/H]^{chem}$, and $[Fe/H]^{chem}$ for 37819 RAVE spectra with STN > 20. The metallicity $[m/H]^{chem}$ is inferred from the chemical elemental abundances with the equation given by Salaris et al. (1993)

$$[m/H]^{chem} = [Fe/H] + \log(0.638 \times 10^{[\alpha/Fe]} + 0.362), \quad (2)$$

where the α-enhancement is computed as

$$[\alpha/Fe] = \frac{[Mg/H] + [Si/H]}{2} - [Fe/H] \quad (3)$$

and the elemental abundances [Mg/H], [Si/H], and [Fe/H] come from the chemical pipeline.

$[m/H]^{RAVE}$ is ∼0.1 dex lower than $[m/H]^{chem}$, which is to be expected as the non-calibrated RAVE metallicity is underestimated by ∼0.15 dex with respect to the reference stars used in Siebert et al. (2011). The shape of the $[m/H]^{RAVE}$ distribution is fairly similar to the $[m/H]^{chem}$ distribution for dwarf stars but different for giants. Moreover, $[m/H]^{RAVE}$ seems to better match $[Fe/H]^{chem}$ than $[m/H]^{chem}$, particularly for giants. This could be due to α-enhancement: giant stars have a higher proportion of thick disk stars (α enhanced) than do dwarf stars, which are mostly thin disk (not α enhanced). Although used during the stellar parameters estimation process, the RAVE pipeline is unable to measure α-enhancement (Zwitter et al. 2008). Therefore, it is possible that particularly for α enhanced stars $[m/H]^{RAVE}$ better represents [Fe/H]. Apart from the discussed shift of 0.1 dex in metallicity, there seems to be fair agreement between the $[m/H]^{RAVE}$ and $[m/H]^{chem}$ distributions.

4. DISCUSSION

For each element, the accuracy of the abundance estimate depends on the number of lines that are strong enough to be clearly detected; to be measurable, the lines must be stronger than the noise. At the same time, the intensity of the lines depends on the stellar parameters and elemental abundances of the star. This means that for a fixed S/N, the accuracy of the elemental abundance is a function of the stellar parameters and of the abundance itself.

The interplay of these factors makes the accuracy of the abundance results difficult to estimate. At high S/N, the accuracy varies from element to element, depending on the number and intensity of the lines measured. For instance, Ti and Ni lines are measured better in stars with $T_{\rm eff}$ lower than ∼5000 K, whereas sulfur (not present in this data release) can be seen and measured only for temperatures higher than ∼4800 K. The RAVE line list has a few weak Ca I lines that can be measured only in stars with [m/H] > -0.5 dex.

Noise affects the EWs of the lines and so the model spectrum. As the pipeline varies the abundances of the individual elements, the larger the number the absorption lines of an element, the lower the abundance error due to the fitting, because the effects of noise are averaged over the lines. Thus, the abundance accuracy of elements with fewer lines is especially affected by noise. When the noise is particularly strong with respect to the intensity of the lines, i.e., low S/N, the minimization routine fits the noise and the resulting elemental abundance diverges. In such cases the pipeline rejects the measurement and renders a null value −9.99.

The situation get worse in the low S/N regime, because the pipeline measures even fewer lines, i.e., only those strong enough to be detected despite the noise. This decreases the number of measurable elements and increases the uncertainties. In Section 3.1, we tested the pipeline down to S/N = 20 to see if at such a low S/N the measurements are still trustworthy. The results suggest we can use such data, but with care. Noise generates selection effects: spectra having low [m/H] or high $T_{\rm eff}$ do not have lines strong enough to overcome the noise and they go through the pipeline unmeasured. A limited number of lines can also generate systematic errors because the abundance of an element depends on just a few lines (sometimes even only one) and thus becomes especially vulnerable to uncertainties in the oscillator strengths.

Nevertheless, the tests performed with synthetic spectra at S/N = 20 show that abundances of elements with strong lines like Fe, Al, and Si can still be measured. At such low S/N, errors as large as ∼0.2–0.3 dex are expected, but they do not show large systematic biases and the residuals are on average close to zero.

We conclude that elemental abundances may be trusted down to S/N = 40 for seven elements (details will follow in Section 5), whereas between S/N = 20 and 40 we can trust the abundance of [Fe/H] and (to be on the safe side) the abundance [α/H], when computed from the average of Mg and Si. Abundances for other elements for the low S/N stars should be considered indicative and used only for exploratory purposes until new comparison stars enable a proper validation of our results in this S/N regime.

4.1. Zero Point of the RAVE Elemental Abundance Scale

Our elemental abundance measurements are indirect measurements in the sense that they are inferred from the comparison between the intensity of lines seen in real spectra and their intensity predicted by stellar atmosphere models. Since the models are different for different stellar parameters, a question arises regarding whether all the models yield elemental abundances which refer to the same zero point, i.e., the origin of the internal elemental abundance scale. The same question concerns whether this zero point refers to the same zero point of the real spectra, i.e., between the internal and external scales.

The latter question has a prompt answer: we do not know the external scale, because real stellar atmospheres have never been directly probed and all elemental abundance measurements refer to models. Therefore, we can only check the consistency of the internal scale. This can be performed by comparing the measured elemental abundances of a sample of synthetic spectra at different stellar parameters, as done in Figure 6.

In this plot, at S/N = 100, the residuals between measured and expected elemental abundances are on average zero for any gravity and metallicity; the points align along a straight line with slope roughly equal to one. This means that the measured differences in elemental abundance at any metallicity regime are the same (constant offset), i.e., they refer to the same zero point. However, the offset from element to element may vary, showing that the offsets are due to the measurement process and not due to the metallicity of the atmosphere models.

On the other hand, there is a clear correlation between residuals and $T_{\rm eff}$: the higher the $T_{\rm eff}$, the higher the measured elemental abundance. This systematic may be due to continuum correction: cooler stars have spectra that are crowded with absorption lines and so the continuum appears lower than it is. Additionally, the varying behavior of the elements in Figure 6 can be explained by considering that their lines lie in different regions of the spectrum, i.e., on the wings of a Ca II line or in a region relatively free of lines. This can translate into systematic, wavelength-localized shifts of the estimated continuum as a function of $T_{\rm eff}$.

Although this systematic effect appears tractable and correctable, we did not apply any correction to the data because such a systematic is not visible on tests with real spectra. When the RAVE elemental abundances are compared with the expected elemental abundances of standard stars as function of $T_{\rm eff}$ no clear trend is visible (Figure 16), except that RAVE elemental abundances have a slight systematic bias to lower values. A reasonable explanation is that the elemental abundance measurements given by SG05 and R10 suffer from the same systematic error, due to uncertainties in estimating the correct continuum level in regions crowded with absorption lines or affected by the wings of strong, broad lines.

We conclude that the RAVE chemical pipeline can determine chemical elemental abundances with a systematic error that may be as large as ∼0.1 dex as a function of $T_{\rm eff}$. Since this systematic looks quite linear with $T_{\rm eff}$ (see Figures 9 and 16) to reduce this error to ±0.05 dex we suggest analyzing separately samples of stars with $T_{\rm eff} > 5500$ K (mostly dwarfs) from samples with $T_{\rm eff} < 5500$ K (mostly giants).

5. THE RAVE CHEMICAL CATALOG

We present the catalog of chemical elemental abundances for 36,561 RAVE stars, measured using 37,848 spectra.

5.1. Sample Selection

The spectra have been selected from the DR3 RAVE database using the following constraints.

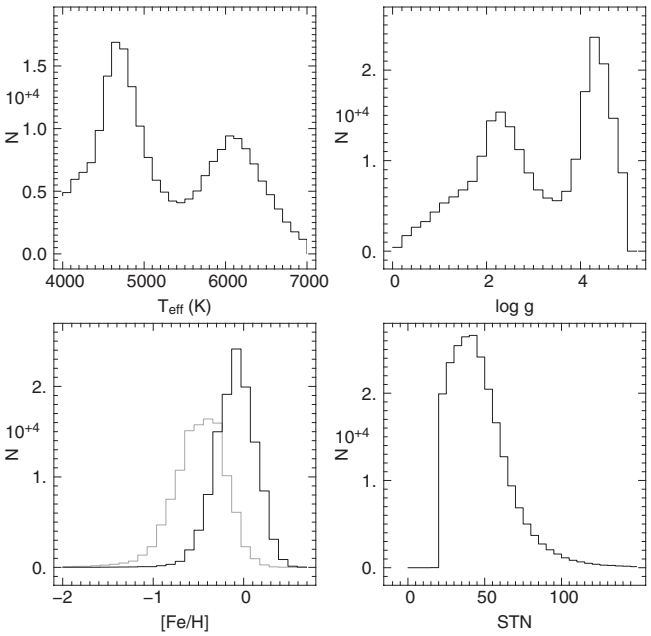

Figure 17. Distributions of stellar parameters $T_{\rm eff}$, log g, [Fe/H], and signal-to-noise ratio STN for 37848 spectra of the chemical catalog. In the bottom left panel, the [Fe/H] distribution is given separately for dwarfs (black line) and giants (gray line).

1. *Effective temperature 4000* $\leqslant$ $T_{\rm eff}(K)$ $\leqslant$ *7000*. This is the temperature range within which the RAVE line list has been calibrated. At lower temperature the spectra are characterized by molecular lines other than CN (CH, TiO, and other molecules), while at higher temperatures lines of ionized atoms appear, and both are not included in the line list.
2. *Signal-to-noise STN* $>$ *20*. For STN $<$ 20 the absorption lines are strongly affected by noise and the stellar parameters and chemical elemental abundances are not reliable.
3. *Rotational velocity* $V_{\rm rot}$ $<$ *50 km* s^{-1}. At higher rotational velocity the lines have an FWHM larger than that due to the spectral resolution (FWHM $\simeq$ 1.2 Å) and they cannot be precisely measured. Moreover, any spectra showing larger lines might be a double-lined spectrum, which also must be avoided.

Despite these selection criteria, some spectra exhibit emission or are affected by bad continuum normalization. For such spectra the stellar parameters and chemical elemental abundances are not reliable and it is advisable to reject them. Constraints on the parameters χ^2 and *frac* help identify these spectra. For statistical studies we suggest rejecting spectra with $\chi^2 > 2000$ and *frac* < 0.7, which removes 739 out of 37,848 spectra of the catalog.

5.2. Stellar Parameters

The distributions of the stellar parameters and STN values are presented in Figure 17. The quantities $T_{\rm eff}$ and log g are given by the RAVE data archive whereas STN and [Fe/H] are estimated by the chemical pipeline. The distributions in $T_{\rm eff}$ and log g show two peaks corresponding to giants at lower temperature and dwarfs, which are mostly at higher temperatures. The iron abundance distribution peaks at [Fe/H] $\simeq -0.1$ dex for dwarfs and [Fe/H] $\simeq -0.5$ dex for giants. The latter are in average more metal-poor because they lie further from the Galactic plane and have therefore a larger fraction of thick disk stars.[23]

5.3. Chemical Elemental Abundances: Selection Effects due to STN and Stellar Parameters

We encourage the user to pay particular attention to selection effects introduced by the stellar parameters and STN. Together they affect the total number of abundance estimations as well as their accuracy. Absorption lines can be undetectable because of the low [m/H] of the star, because the too-high (or too-low) $T_{\rm eff}$ does not populate enough of its electronic levels, or because the spectrum has a too-low STN. This is illustrated in Figures 18 and 19, where the number of spectra having [X/H] estimation diminishes with STN and [m/H]. In general, only metal-rich stars have elemental abundance estimations at any STN whereas metal-poor stars have estimations only if their spectra have high STN.

5.4. Accuracy and Reliability Element by Element

We now discuss and summarize the reliability of the chemical abundances for individual elements in light of the previous

[23] As RAVE is a magnitude limited survey, the intrinsically bright objects are on average at large distances.

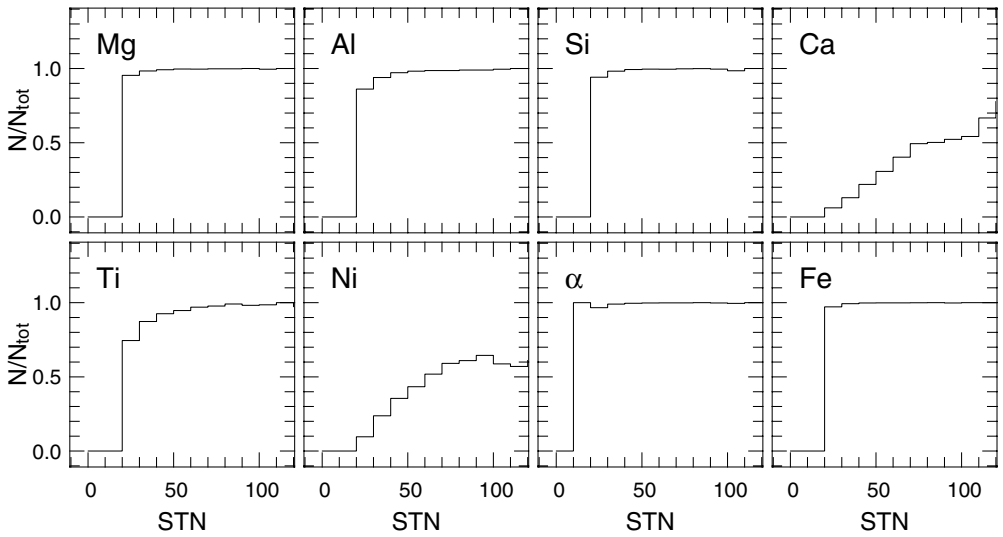

Figure 18. Fraction of spectra having elemental abundance measurements as a function of the STN. Every bin is normalized to the total number of observed spectra in the corresponding STN bin.

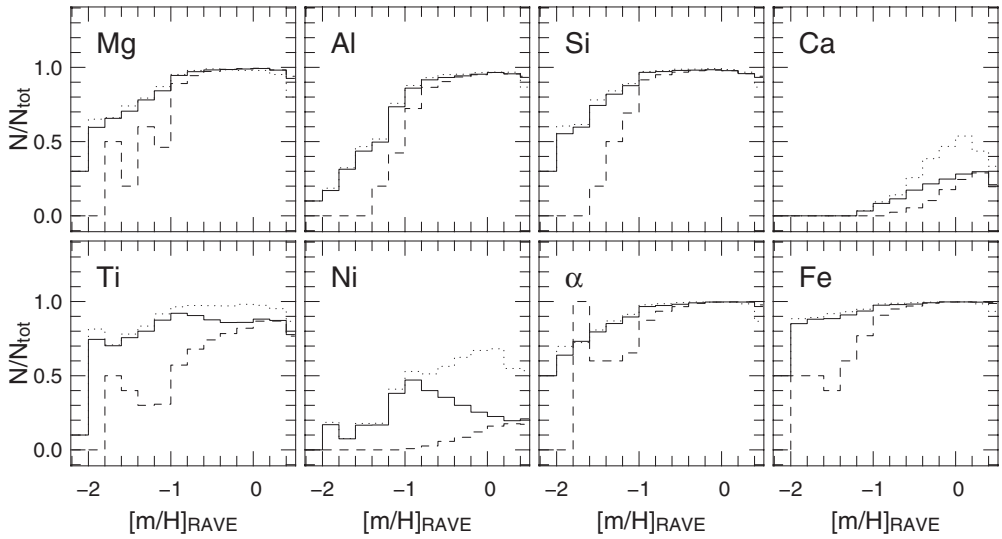

Figure 19. Fraction of spectra having elemental abundance measurements as a function of $[m/H]^{RAVE}$. Every bin is normalized to the total number of observed spectra in that $[m/H]^{RAVE}$ bin. The solid, dashed, and dotted lines represent the whole sample, dwarf stars only, and giants stars only, respectively.

Table 2
Catalog Description

Field Number	Name	Null Value	Description
1	RAVEID	...	RAVE target designation
2	Name	...	Target designation
3	Obsdate	...	Date of observation yyyymmdd
4	FieldName	...	Name of RAVE field
5	FiberNumber	...	Fiber number [1, 150]
6	[Mg/H]	−9.99	Mg abundance
7	*N*	...	Number of Mg lines measured
8	[Al/H]	−9.99	Al abundance
9	*N*	...	Number of Al lines measured
10	[Si/H]	−9.99	Si abundance
11	*N*	...	Number of Si lines measured
12	[Ca/H]	−9.99	Ca abundance
13	*N*	...	Number of Ca lines measured
14	[Ti/H]	−9.99	Ti abundance
15	*N*	...	Number of Ti lines measured
16	[Fe/H]	−9.99	Fe abundance
17	*N*	...	Number of Fe lines measured
18	[Ni/H]	−9.99	Ni abundance
19	*N*	...	Number of Ni lines measured
20	$T_{\rm eff}$	...	RAVE effective temperature
21	$\log g$	...	RAVE gravity
22	$[m/H]^{RAVE}$	...	RAVE metallicity
23	$[m/H]^{chem}$	...	Metallicity from the chemical pipeline
24	$[\alpha/Fe]^{chem}$	...	α-enhancement from the chemical pipeline
25	STN	...	Signal-to-noise ratio
26	frac	...	Fraction of spectrum matching the template well
27	Ntot	...	Total number of lines measured
28	χ^2	...	χ^2 between observed and template spectra

(This table is available in its entirety in machine-readable and Virtual Observatory (VO) forms in the online journal. A portion is shown here for guidance regarding its form and content.)

discussion. First, we make some general remarks about the measured elemental abundances and their errors.

1. The accuracy of the chemical abundances depends on several variables. In particular if $T_{\rm eff}$ is erroneously estimated, the abundances are affected to different degree for different elements. If there are systematics deviations in $T_{\rm eff}$ there will be systematic deviations in [X/H] as well.
2. In general [X/H] are underestimated, and the magnitude of the bias is a function of $T_{\rm eff}$: stars with $T_{\rm eff} < 5000$ K yield on average abundances that are ∼0.1 dex lower than stars with >5000 K, whose abundance errors average to zero. This effect increases the errors when stars with different $T_{\rm eff}$ are analyzed. On the other hand, *relative abundances [X/Fe] are nearly unaffected because the trend is similar for all elements*.

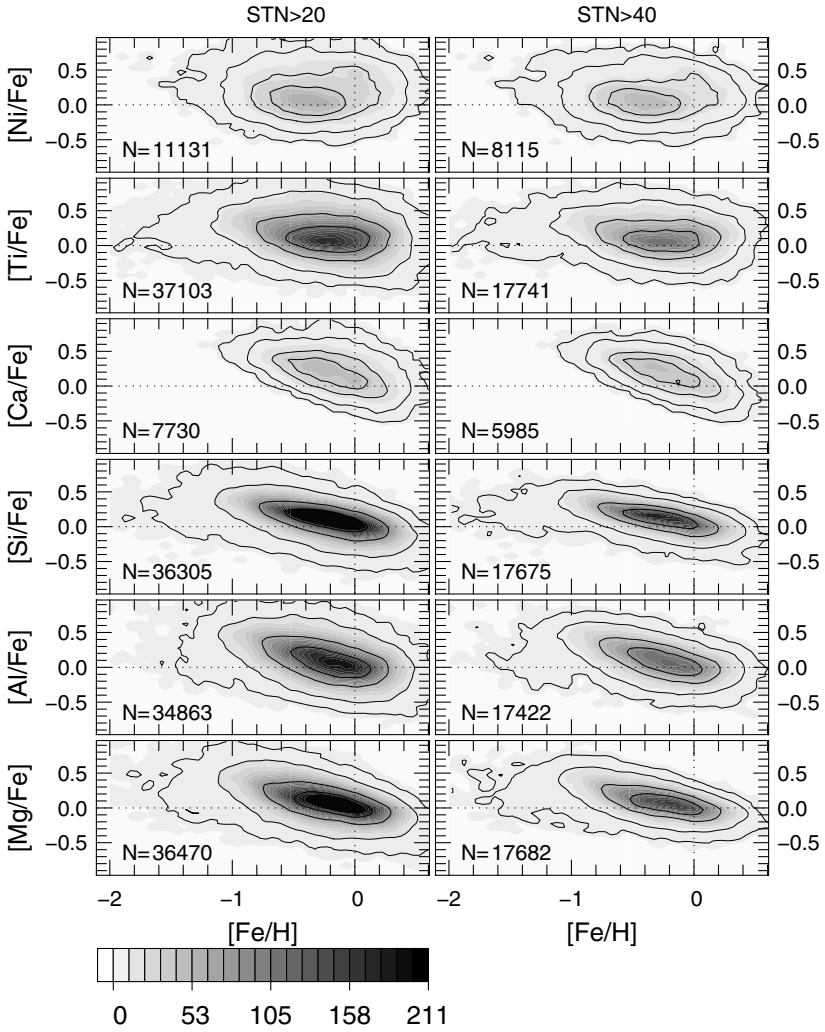

Figure 20. Abundances relative to iron for spectra with STN > 20 (left panels) and STN > 40 (right panels). The isocontours hold 34.0%, 68.0%, 95.0%, and 99.5% of the sample.

3. The errors given below refer to the expected errors for two intervals of STN at [m/H] ∼ 0.0 dex. As already discussed in the previous section, errors can increase for lower STN and lower [m/H].

Magnesium yields reliable results on synthetic and real spectra. At any $T_{\rm eff}$ we expect an abundance error $\sigma_{\rm Mg} \leqslant 0.15$ dex for STN $\geqslant 40$ and ∼0.25 dex for $20 \geqslant$ STN $\geqslant 40$.

Aluminum abundances are obtained from only two physically isolated lines (which are instrumentally blended at RAVE resolution). Despite the instrumental blending, the lines are strong and give accurate estimates in tests with synthetic and real spectra that shows no systematic offset. For STN $\geqslant 40$ we expect abundance errors $\sigma_{\rm Al} \leqslant 0.2$ dex and ∼0.3 dex for $20 \geqslant$ STN $\geqslant 40$.

Silicon is the most reliable element together with Fe. We expect an abundance error $\sigma_{\rm Si} \leqslant 0.15$ dex for STN $\geqslant 40$ and ∼0.20 dex for $20 \geqslant$ STN $\geqslant 40$.

Calcium abundances are obtained from only five weak Ca I lines. Ca I is better measured at higher metallicity and $T_{\rm eff} <$ 5000 K. Estimated errors are $\sigma_{\rm Ca}$ ∼0.25 dex for STN $\geqslant 40$ and ∼0.4 dex for $20 \geqslant$ STN $\geqslant 40$.

Titanium gives reliable abundances at high STN. At STN ∼ 40 its abundance is reliable for $T_{\rm eff} <$ 5000 K and underestimated for higher temperatures. The correlation with $T_{\rm eff}$ errors is particularly strong ($T_{\rm eff}$ underestimation generates [Ti/H] underestimation and vice versa) leading to larger errors. We expect an abundance error of $\sigma_{\rm Ti} \sim 0.2$ dex at STN $\geqslant 40$ and ∼ 0.3 dex for $20 \geqslant$ STN $\geqslant 40$. We recommend separately analyzing stars with $T_{\rm eff}$ lower and higher than 5000 K.

Iron is the most reliable element together with Si. It can be accurately measured on spectra with any $T_{\rm eff}$ in the range we consider. We expect an abundance error of $\sigma_{\rm Fe} \sim 0.1$ dex at STN $\geqslant 40$ and ∼0.2 dex at $20 \geqslant$ STN $\geqslant 40$.

Nickel has six weak lines in the RAVE wavelength range that are visible only at $T_{\rm eff} <$ 5000 K. In synthetic spectra with STN = 100 the pipeline yields errors comparable to those of other elements but biased to lower values by ∼0.2 dex. It is not measurable for [m/H] < -0.6 dex. Tests on real spectra are inconclusive because they were all performed for stars with $T_{\rm eff} >$ 5000 K. We expect uncertainties of $\sigma_{\rm Ni} \sim 0.2$ dex for STN $\geqslant 40$ and ∼0.3 dex for $20 \geqslant$ STN $\geqslant 40$. Because of the small number and the weakness of its lines, it is advisable to use Ni values with care.

The *overall metallicity* $[{\rm m/H}]^{\rm chem}$ is inferred from the chemical elemental abundances with Equation (2) (Salaris et al. 1993), with the abundances [Mg/H], [Si/H], and [Fe/H] delivered by the chemical pipeline. The metallicity $[{\rm m/H}]^{\rm chem}$ is reliable and we expect errors of $\sigma_{\rm [m/H]} \sim 0.1$ dex for STN $\geqslant 40$ and ∼0.2 dex for $20 \geqslant$ STN $\geqslant 40$.

The α-enhancement [α/Fe] has been computed as the average of [Mg/Fe] and [Si/Fe] (Equation (3)). In the range 20 ⩾ STN ⩾ 40 it is advisable to use it instead of the single α element values because it is more reliable. We estimate errors of $\sigma_\alpha \sim 0.1$ dex for STN ⩾ 40 and ∼0.2 dex for 20 ⩾ STN ⩾ 40.

5.5. The Data

The RAVE chemical catalog contains data for 37,848 spectra of 36,561 stars and it is provided as an ASCII table of 37,848 lines. It contains chemical abundances for the elements Mg, Al, Si, Ca, Ti, Fe, and Ni, RAVE stellar parameters, signal-to-noise STN, object name, and other parameters for quality checks as explained in Table 2. The distributions of the relative chemical abundances are shown in Figure 20. The catalog will be accessible online at http://www.rave-survey.org and via the Strasbourg Astronomical Data Center (CDS) service.

6. CONCLUSIONS

This first release of the RAVE chemical catalog reports the chemical abundances of seven elements (Mg, Al, Si, Ca, Ti, Fe, Ni) for 36,561 stars (from 37,848 spectra) selected from the DR3 data release. The chemical processing pipeline developed for the creation of the present catalog assures homogeneous elemental abundance measurements in addition to the RAVE pipeline that estimates the values of the stellar parameters and radial velocities.

The uncertainties in the estimated elemental abundances depend mostly on the signal-to-noise ratio (STN) of the spectra, on the values of the stellar parameters of the stars, and on the element considered. The expected errors in abundance can be as small as 0.1 dex at STN > 80 for the elements Fe and Si and up to ∼0.3 at 20 ⩾ STN ⩾ 40 for Ni.

On average we expect errors of ∼0.2 dex at STN ⩾ 40 for most of the elements. The relative abundances [X/Fe] are reliable with an underestimation of ∼−0.1 dex for [X/Fe] > +0.3.

We plan to increase the number of measured elements in future data releases. We believe that with further development of the chemical pipeline it should be possible to enrich the catalog with the abundances of at least two other elements (oxygen and sulfur).

The availability of chemical elemental abundances, together with the radial velocities of the stars (given in the RAVE DR3 data release) and their distances (Breddels et al. 2010; Zwitter et al. 2010; Burnett et al. 2011), makes RAVE a prime data set for Galactic archaeology investigations.

C.B. thanks M. Asplund, D. Yong, and F. Thévenin for the useful discussions he had with them.

Funding for RAVE has been provided by the Australian Astronomical Observatory; the Lebniz-Institut fr Astrophysik Potsdam (AIP); the Australian National University; the Australian Research Council; the European Research Council through ERC-StG 240271 (Galactica); the French National Research Agency; the German Research Foundation (DFG); the Sonderforschungsbereich "The Milky Way System" (SFB 881) of the DFG; the Istituto Nazionale di Astrofisica at Padova; The Johns Hopkins University; the National Science Foundation of the USA (AST- 0908326); the W. M. Keck foundation; the Macquarie University; the Netherlands Research School for Astronomy; the Natural Sciences and Engineering Research Council of Canada; the Slovenian Research Agency; the Swiss National Science Foundation; the Science & Technology Facilities Council of the UK; Opticon; Strasbourg Observatory; and the Universities of Groningen, Heidelberg, and Sydney.

The RAVE Web site is at http://www.rave-survey.org.

APPENDIX A

CORRECTION OF THE ATOMIC OSCILLATOR STRENGTHS IN THE RAVE/*Gaia* WAVELENGTH REGION

In the following we outline how the pipeline treats oscillator strengths (gf, often expressed as a logarithm $\log gf$) in the wavelength range 8400–8800 Å. These are necessary in order to obtain trustworthy elemental abundance measurements in a wavelength region which is still poorly known. According to the VALD [1999] only 11 Fe lines have accurate gf-value laboratory measurements (Blackwell et al. 1986; Bard et al. 1991; Bard & Kock 1994), while the remaining hundreds of lines rely on theoretical and semi-empirical calculations (Kurucz 1995). Some of these values have proved imprecise, with errors as large as 1 dex for important lines belonging to Fe and Si (Bigot & Thévenin 2006). We have attempted to improve the oscillator strength values of 604 absorption lines using an inverse spectral analysis applied to spectra of the Sun and Arcturus.

A.1. Method

The RAVE line list consists of 604 absorption lines (excluding the H I and Ca II strong lines) identified by looking at the high S/N Sun and Arcturus spectra (Hinkle et al. 2000) and verified by cross checking the line identification of Moore et al. (1966) and Hinkle et al. (2000). Some previously unidentified lines have been added in order to match features that are clearly visible in spectra of the Sun and Arcturus.

The lines have been selected from Kurucz data (Kurucz 1995) and we have also adopted Kurucz's wavelengths and excitation potentials χ. Following Chen et al. (2000) we also adopted the enhancement factor E_γ for the Unsöld approximation because it is commonly accepted that the line broadening due to Van der Waals interaction obtained from Unsöld's approximation is too weak and needs to be corrected. For the CN molecule we used the dissociation energy $D = 7.75$ eV, as suggested by Sauval & Grevesse (1994).

We performed the inverse spectral analysis by synthesizing solar and Arcturus's spectra with MOOG (a standard LTE line analysis and synthesis code by Sneden 1973) and changing the $\log gf$s values until a good match with both observed spectra is reached. We show here that matching these two spectra (or more) allows us to improve the $\log gf$s of blended lines, which otherwise would be impossible to disentangle.

The EW of a measured absorption line is related to the $\log gf$-value through the curve of growth equation (see Gray 2005, formula 16.4)

$$\log \frac{\mathrm{EW}}{\lambda} = \log C + \log A + \log(gf \cdot \lambda) - \theta\chi - \log \kappa_\nu, \quad \text{(A1)}$$

where C and θ are functions[24] of the temperature T, and κ_ν is the opacity at the frequency ν. When all the atmosphere model

[24] C and θ are expressed as follows
$C = \text{constant} \cdot \frac{\pi e^2}{mc^2} \frac{N_j/N_E}{u(T)} N_\mathrm{H}$,
$\theta = 5040/T$,
where T is the temperature, N_j/N_E is the fraction of atoms of the jth stage of ionization with respect to the number of atoms of the element considered, N_H is the number of hydrogen atoms per unit volume, and $u(T)$ is the partition function.

parameters are fixed, the curve of growth equation can be written as a function, f, of $\log gf$ and elemental abundance A

$$\mathrm{EW} = f(\log gf, A). \quad \text{(A2)}$$

This allows us to disentangle two or more blended lines: let $\mathrm{EW}^x_{\mathrm{blend}}$ be the EW of a blended feature of the star x composed of n lines of m different elements ($n \geqslant m$) and having $\mathrm{EW}_1, \mathrm{EW}_2, ..., \mathrm{EW}_n$ unknown EWs. Then we can write the system of equations

$$\begin{aligned} \mathrm{EW}^1_{\mathrm{blend}} &= \sum^{n} f(\log gf_n, A_n) \quad \text{(A3)} \\ \mathrm{EW}^2_{\mathrm{blend}} &= \sum^{n} f(\log gf_n, A_n) \\ &\vdots \quad \vdots \\ \mathrm{EW}^N_{\mathrm{blend}} &= \sum^{n} f(\log gf_n, A_n), \end{aligned}$$

where A_n represents the abundance of the element the line belongs to.

Since the physical conditions and elemental abundance A of each stars are in general different, the values $\mathrm{EW}^x_{\mathrm{blend}}$ are different as well. The equation system A3 is solvable when the (N) number of equations is greater than the unknown $n+m$. The existence and uniqueness of the solution is assured even for lines where the weak-line approximation does not hold, because the first derivative of the curve of growth is always positive.

This means that it is always possible to determine the $\log gf$s of a blended feature and the elemental abundances by using a large enough number of spectra of different stars. In our case we have used two spectra: the Sun and Arcturus.

A.2. The Correction Routine

The following routine is valid when the stellar parameters and elemental abundances of both stars are known. We also consider later the case where elemental abundances are not known. To synthesize the solar spectrum we assumed an effective temperature $T_{\mathrm{eff}} = 5777$ K, gravity $\log g = 4.44$, microturbulence $V_t = 1.0\,\mathrm{km\,s^{-1}}$, and metallicity $[\mathrm{m/H}] = 0.00$. For Arcturus the atmospheric parameters are taken from Earle et al. (2005) ($T_{\mathrm{eff}} = 4340$ K, $\log g = 1.93$, $V_t = 1.87$ km s^{-1}, $[\mathrm{m/H}] = -0.55$ dex).

The synthetic spectra have been obtained assuming solar chemical abundances by Grevesse & Sauval (1998, hereafter GS98) and adopting the grid ATLAS9 model atmospheres of Castelli & Kurucz (2003). The $\log gf$s correction is performed using the following procedure.

1. Synthesize the solar and Arcturus spectra from our line list.
2. Select the first line of the list.
3. Integrate the absorbed flux of the observed and synthesized spectra over an interval spanning 0.4 Å around the center of the line (roughly 1 FWHM, which takes into account most of the absorbed flux) and calculate the normalized EW residual (NEWR), defined as follows

$$\mathrm{NEWR} = \frac{(F_{\mathrm{synt}} - F_{\mathrm{obs}})}{F_{\mathrm{obs}}}, \quad \text{(A4)}$$

where F_{synt} and F_{obs} are the flux of the synthetic and the observed spectrum, respectively. For the Sun and Arcturus we write ($\mathrm{NEWR_{Sun}}$) and ($\mathrm{NEWR_{Arc}}$).

Table 3
Arcturus's Elemental Abundances Compared with the Results by Luck & Heiter (2005, hereafter LH05), Thévenin (1998, hereafter T98), and Fulbright et al. (2007, hereafter F07)

Abundance	This Work	LH05	T98	F07
[O/H]	+0.17		−0.30	−0.10
[Mg/H]	−0.03	+0.02	−0.45	−0.10
[Al/H]	−0.27	−0.28	−0.40	−0.17
[Si/H]	−0.15	−0.14	−0.30	−0.15
[S/H]	−0.13			
[Ca/H]	−0.26	−0.56	−0.20	−0.28
[Ti/H]	−0.22	−0.39	−0.20	−0.20
[Cr/H]	−0.37	−0.55	−0.20	
[Fe/H]	−0.52	−0.55	−0.40	−0.54
[Co/H]	−0.17	−0.36	−0.20	
[Ni/H]	−0.45	−0.48	−0.35	
[Zr/H]	−1.00			

4. If $\mathrm{NEWR_{Sun}} < -0.05$ then add +0.01 to the $\log gf$, else if $\mathrm{NEWR_{Sun}} > 0.05$ then add −0.01 to the $\log gf$ (i.e., match the Sun first). Go to step 7.
5. If $|\mathrm{NEWR_{Sun}}| < 0.05$ and $\mathrm{NEWR_{Arc}} < -0.05$ then add −0.01 to the $\log gf$, else if $|\mathrm{NEWR_{Sun}}| < 0.05$ and $\mathrm{NEWR_{Arc}} > 0.05$ then add +0.01 to the $\log gf$ (e.g., if the Sun matches then try to match Arcturus). Go to step 7.
6. If $|\mathrm{NEWR_{Sun}}|$ and $|NEWR_{\mathrm{Arc}}|$ are both <0.05 then a valid $\log gf$ has been reached.
7. Select the next line from the line list and return to step 3.

The routine is iterated until no more improvement is seen. For about 10 lines a good match could not be reached. Several reasons may be behind this: bad continuum correction, lines located over the Ca II lines where the fit is inaccurate, misidentified lines, or unrecognized blends. For these lines, we did a visual check and manually corrected the $\log gf$ values. The correction is good enough to derive gf values that yield abundance errors per measured line smaller than 0.2 dex in average for both the Sun and Arcturus.

Since the abundance of Arcturus is not known for all elements, we decided to assume an initial abundance for all the elements ([X/H] = [m/H]) and find the right abundances with the following procedure.

1. Synthesize the Sun's and Arcturus's spectra.
2. Correct the $\log gf$-values by running the above correction routine until no more improvements are possible.
3. Check the distribution of the NEWRs for each element separately: if a positive/negative offset is present, decrease/increase its abundance.
4. Synthesize the solar and Arcturus's spectra with the new $\log gf$s and abundances.
5. Return to step 2.

This algorithm is repeated until there are no more improvements. The results of this procedure are the new $\log gf$s and Arcturus's chemical abundances (listed in Table 3).

A.2.1. Multiplets Treatment

In the RAVE/*Gaia* wavelength range there are features that belong to atomic multiplets. An interesting characteristic of these multiplets is that they share the same excitation potential χ and have small differences in wavelength. In this case, obtaining a proper $\log gf$ for the individual lines is problematic.

Table 4
Seven Lines Extracted from the RAVE Line List

Wavelength (Å)	Atomic Species	χ (eV)	$\log gf$	E_γ	Dissociation Energy (eV)
8643.306	26.0	4.913304	−2.470	1.40	0.00
8644.077	607.0	0.933782	−1.773	2.50	7.75
8646.050	607.0	1.324726	−1.540	2.50	7.75
8646.371	14.0	6.206423	−1.740	1.30	0.00
8647.175	607.0	0.877831	−1.872	2.50	7.75
8648.465	14.0	6.206423	0.100	1.30	0.00
8648.688	607.0	0.910915	−1.516	2.50	7.75

Notes. The whole table contains 604 lines with $\log gf$ correction, and the 3 Ca II and 8 H I lines which are not used for elemental abundance measurements (and did not undergo to $\log gf$ corrections). The atomic species 607.0 represent the CN molecule, following the MOOG format.

(This table is available in its entirety in machine-readable and Virtual Observatory (VO) forms in the online journal. A portion is shown here for guidance regarding its form and content.)

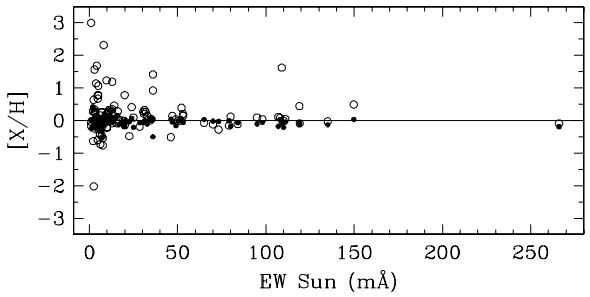

Figure 21. Solar elemental abundances obtained from 100 atomic lines for which EWs (x-axis) have been measured by hand from the solar spectrum. The open points represent the elemental abundances obtained by using the Kurucz gf-values, whereas the corrected gf-values are represented by the solid points. The respective dispersions are $\sigma = 0.63$ dex (open points) and $\sigma = 0.15$ dex (solid points).

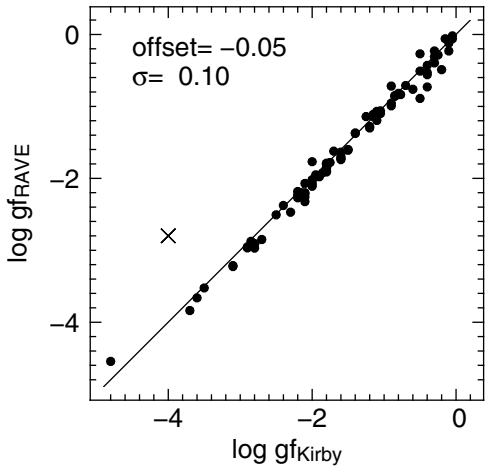

Figure 22. Comparison between corrected $\log gf$s by Kirby et al. 2008 (x-axis) and RAVE (y-axis). The statistics on the panel refers to points after the crossed outlier has been removed.

We work around this problem in the following way: consider the two Al I lines at $\lambda_1 = 8773.896$ Å and $\lambda_2 = 8773.897$ Å that share the same excitation potential $\chi = 4.021947$ eV. The two lines have unknown equivalent widths EW_1 and EW_2 but the sum

$$EW_{Tot} = EW_1 + EW_2, \tag{A5}$$

is measured and well known. We can write the curve of growth as

$$\frac{EW}{\lambda} = \frac{C \cdot A_{Al} \cdot (gf) \cdot \lambda}{10^{\theta\chi} \cdot \kappa_\nu}, \tag{A6}$$

where A_{Al} is the aluminum abundance and the other quantities are as in Equation (A1). Substituting Equation (A6) into Equation (A5) and adopting the approximation $\lambda_1 \simeq \lambda_2 = \lambda$ we obtain

$$\frac{EW_{Tot}}{\lambda} = \frac{EW_1 + EW_2}{\lambda} = \frac{C \cdot A_{Al} \cdot (gf_1 + gf_2) \cdot \lambda}{10^{\theta\chi} \cdot \kappa_\nu}. \tag{A7}$$

Using the logarithmic form, this equation then becomes

$$\log \frac{EW_{Tot}}{\lambda} = \log C + \log A + \log((gf_1 + gf_2) \cdot \lambda) - \theta\chi - \log \kappa_\nu, \tag{A8}$$

which suggests that an appropriate functional form for a "dummy" variable $\log gf_d$ would be $\log(gf_1 + gf_2)$. Even if this does not allow us to disentangle the two $\log gf$s, we can consider the multiplet as if it were one single line and correct the $\log gf_{fic}$; it will be a "dummy" value but it results in giving the correct abundance of Al. This correction has also been applied to three Mg I multiplets, centered at wavelengths 8717.814, 8736.020, and 8773.896 Å.

A.3. Tests

In order to test the accuracy of this procedure, we have measured by hand the EWs of 100 atomic lines in the solar spectrum. Figure 21 presents the difference in abundances obtained by using the Kurucz gf values (open points) and the corrected ones (solid points). Our correction reduced the standard deviations of the abundance residuals from $\sigma = 0.63$ dex to $\sigma = 0.15$ dex and their averages from +0.16 to −0.05.

We also compared our results to the $\log gf$ by Kirby et al. (2008), who corrected the gf values by applying a similar method, i.e., by synthesizing the solar and Arcturus's spectra and comparing the synthetic spectra with the observed ones. A comparison between our and their results is shown in Figure 22 for the 89 corrected lines in common: on average our $\log gf$ are lower by −0.05 dex. This is very likely due to different solar elemental abundances adopted: Kirby adopts the Anders & Grevesse (1989) abundances which are on average higher than Grevesse & Sauval (1998), which we adopt.

One more test involves comparing our results for Arcturus's elemental abundances with abundances quoted in the literature.

This is done in Table 3 where our elemental abundances are compared with those of Luck & Heiter (2005), Thévenin (1998, hereafter T98), and Fulbright et al. (2007, hereafter F07). From the consistency of these tests, we are confident that our computed $\log gf$ values are accurate and that our procedure yields robust and reliable elemental abundance estimates. In Table 4 we outline the final RAVE line list with the obtained $\log gf$.

APPENDIX B

MICROTURBULENCE

The polynomial function used to determine the microturbulence ξ is expressed as follows:

$$\xi_{\rm poly}({\rm km\ s^{-1}}) = \sum_{i,j=0,1,2,3}^{i+j\leqslant 3} a_{ij} T^i (\log g)^j, \qquad \text{(B1)}$$

where the coefficients a_{ij} are

$$\begin{aligned} a_{00} &= -10.3533 \qquad \text{(B2)}\\ a_{01} &= 2.59492\\ a_{02} &= 0.161863\\ a_{03} &= 0.176579\\ a_{10} &= 0.00509193\\ a_{11} &= -0.00157151\\ a_{12} &= -3.99782 \times 10^{-7}\\ a_{20} &= -0.000361822\\ a_{21} &= 3.82802 \times 10^{-7}\\ a_{30} &= -5.18845 \times 10^{-11}. \end{aligned}$$

REFERENCES

Allende Prieto, C., Barklem, P. S., Lambert, D. L., & Cunha, K. 2004, A&A, 420, 183
Anders, E., & Grevesse, N. 1989, Geochim. Cosmochim. Acta, 53, 197
Bard, A., & Kock, M. 1994, A&A, 282, 1014
Bard, A., Kock, A., & Kock, M. 1991, A&A, 248, 315
Bensby, T., Feltzing, S., Lundström, I., & Ilyin, I. 2005, A&A, 433, 185
Bigot, L., & Thévenin, F. 2006, MNRAS, 372, 609
Blackwell, D. E., Booth, A. J., Haddock, D. J., Petford, A. D., & Leggett, S. K. 1986, MNRAS, 220, 549
Breddels, M. A., Smith, M. C., Helmi, A., et al. 2010, A&A, 511, 90
Burnett, B., Binney, J., Sharma, S., et al. 2011, A&A, 532, 113
Castelli, F., & Kurucz, R. L. 2003, in IAU Symp. 210, Modelling of Stellar Atmospheres, ed. N. Piskunov, W. W. Wiess, & D. F. Gray (Published on behalf of the IAU by the ASP; Cambridge: Cambridge Univ. Press), 20
Chen, Y. Q., Nissen, P. E., Zhao, G., Zhang, H. W., & Benoni, T. 2000, A&AS, 141, 491
Edvardsson, B., Andersen, J., Gustafsson, B., et al. 1993, A&A, 275, 101
Eggen, O. 1965, in Galactic Structure, Stars and Stellar Systems, Vol. 5, ed. A. Blaauw & M. Schmidt (Chicago: Univ. Chicago Press), 111
Freeman, K., & Bland-Hawthorn, J. 2002, ARA&A, 40, 487
Freeman, K., & Bland-Hawthorn, J. 2008, in ASP Conf. Ser. 399, Panoramic Views of Galaxy Formation and Evolution, ed. T. Kodama, T. Yamada, & K. Aoki (San Francisco, CA: ASP), 439
Fuhrmann, K. 1998, A&A, 338, 161
Fuhrmann, K. 2008, MNRAS, 384, 173
Fulbright, J. P., McWilliam, A., & Rich, R. M. 2006, AJ, 636, 821
Fulbright, J. P., McWilliam, A., & Rich, R. M. 2007, AJ, 661, 1152
Gray, D. F. 2005, The Observation and Analysis of Stellar Photospheres (3rd ed.; Cambridge: Cambridge Univ. Press)
Grevesse, N., & Sauval, A. J. 1998, Space Sci. Rev., 85, 161
Helmi, A., Navarro, J. F., Nordström, B., et al. 2006, MNRAS, 365, 1309
Hinkle, K., Wallace, L., Valenti, J., & Harmer, D. 2000, Visible and Near Infrared Atlas of the Arcturus Spectrum 3727–9300 Å, ftp://ftp.noao.edu/catalogs/arcturusatlas/visual
Høg, E., Fabricius, C., Makarov, V. V., et al. 2000, A&A, 355, L27
Kirby, E. N., Guhathakurta, P., & Sneden, C. 2008, AJ, 682, 1217
Kupka, F., Piskunov, N., Ryabchikova, T. A., Stempels, H. C., & Weiss, W. W. 1999, A&AS, 138, 119
Kurucz, R. L. 1995, in ASP Conf. Ser. 78, Astrophysical Application of Powerful New Database, ed. S. J. Adelman & W. L. Wiese (San Francisco, CA: ASP), 205
Luck, R. E., & Heiter, U. 2005, AJ, 129, 1063
Luck, R. E., & Heiter, U. 2006, AJ, 131, 3069
Luck, R. E., & Heiter, U. 2007, AJ, 133, 2464
Mishenina, T. V., Soubiran, C., Kovtyukh, V. V., & Korotin, S. A. 2004, A&A, 418, 551
Moore, C. E., Minnaert, M. G. J., & Houtgast, J. 1966, The Solar Spectrum 2935 Å to 8770 Å, National Bureau of Standards Monograph (Washington, DC: US Government Printing Office), 61
Nordström, B., Mayor, M., Andersen, J., et al. 2004, A&A, 418, 989
Perryman, M. A. C., de Boer, K. S., Gilmore, G., et al. 2001, A&A, 369, 339
Reddy, B. E., Lambert, D. L., & Allende Prieto, C. 2006, MNRAS, 367, 1329
Reddy, B. E., Tomkin, J., Lambert, L., & Allende Prieto, C. 2003, MNRAS, 340, 304
Robin, A. C., Reylé, C., Derrière, S., & Picaud, S. 2003, A&A, 409, 523
Roeser, S., Schilbach, E., Schwan, H., et al. 2008, A&A, 488, 401
Ruchti, G. R., Fulbright, J. P., Wyse, R. F. G., et al. 2010, ApJ, 721, 92
Salaris, M., Chieffi, A., & Straniero, O. 1993, AJ, 414, 580
Sauval, A. J., & Grevesse, N. 1994, in IAU Symp. 154, Infrared Solar Physic, ed. D. M. Rabin, J. T. Jefferies, & C. Lindsey (Dordrecht: Kluwer), 549
Siebert, A., Williams, M. E. K., Siviero, A., et al. 2011, AJ, 141, 187
Sneden, C. 1973, PhD thesis, Univ. Texas at Austin
Soubiran, C., & Girard, P. 2005, A&A, 438, 139
Soubiran, C., Le Campion, J.-F., Cayrel de Strobel, G., & Caillo, A. 2010, A&A, 515, 111
Steinmetz, M., Zwitter, T., Siebert, A., et al. 2006, AJ, 132, 1645
Thévenin, F. 1998, VizieR On-line Data Catalog: III/193
Valenti, J. A., & Fisher, D. A. 2005, ApJS, 159, 141
Venn, K. A., Irwin, M., Shetrone, M. D., et al. 2004, AJ, 128, 1177
Yanny, B., Rockosi, C., Newberg, H. J., et al. 2009, AJ, 137, 4377
Zacharias, N., Urban, S. E., Zacharias, M. I., et al. 2004, AJ, 127, 3043
Zwitter, T., Matijevič, G., Breddels, M. A., et al. 2010, A&A, 522, 54
Zwitter, T., Siebert, A., Munari, U., et al. 2008, AJ, 136, 421